American Physiological Society | Journal of Neurophysiology

PUBLISHED ARTICLE
ARCHIVES
SUBSCRIPTIONS
SUBMISSIONS
CONTACT US

J Neurophysiol. 2016 Aug 1; 116(2): 825–843.
Published online 2016 May 25. doi: 10.1152/jn.00110.2016
PMCID: PMC4995284

Heat pulse excitability of vestibular hair cells and afferent neurons

Richard D. Rabbitt,[1,*] Alan M. Brichta,[2,*] Hessam Tabatabaee,[2] Peter J. Boutros,[3] JoongHo Ahn,[3] Charles C. Della Santina,[3] Lauren A. Poppi,[2] and Rebecca Lim[2,*]

[1]Departments of Bioengineering and Otolaryngology, University of Utah, Salt Lake City, Utah;
[2]School of Biomedical Sciences and Pharmacy, University of Newcastle, Callaghan, New South Wales, Australia; and
[3]Department of Otolaryngology-Head and Neck Surgery, Johns Hopkins School of Medicine, Baltimore, Maryland
Corresponding author.
[*]R. D. Rabbitt, A. M. Brichta, and R. Lim contributed equally to this work.
Address for reprint requests and other correspondence: R. D. Rabbitt, Depts. of Bioengineering and Otolaryngology, Univ. of Utah, 36 S. Wasatch Dr., SMBB 3100, Salt Lake City, UT 84112 (e-mail: r.rabbitt@utah.edu).

Received 2016 Feb 8; Accepted 2016 May 24.

Abstract

Go to:

In the present study we combined electrophysiology with optical heat pulse stimuli to examine thermodynamics of membrane electrical excitability in mammalian vestibular hair cells and afferent neurons. We recorded whole cell currents in mammalian type II vestibular hair cells using an excised preparation (mouse) and action potentials (APs) in afferent neurons in vivo (chinchilla) in response to optical heat pulses applied to the crista ($\Delta T \approx 0.25$°C per pulse). Afferent spike trains evoked by heat pulse stimuli were diverse and included asynchronous inhibition, asynchronous excitation, and/or phase-locked APs synchronized to each infrared heat pulse. Thermal responses of membrane currents responsible for APs in ganglion neurons were strictly excitatory, with $Q_{10} \approx 2$. In contrast, hair cells responded with a mix of excitatory and inhibitory currents. Excitatory hair cell membrane currents included a thermoelectric capacitive current proportional to the rate of temperature rise (dT/dt) and an inward conduction current driven by ΔT. An iberiotoxin-sensitive inhibitory conduction current was also evoked by ΔT, rising in <3 ms and decaying with a time constant of ~24 ms. The inhibitory component dominated whole cell currents in 50% of hair cells at −68 mV and in 67% of hair cells at −60 mV. Responses were quantified and described on the basis of first principles of thermodynamics. Results identify key molecular targets underlying heat pulse excitability in vestibular sensory organs and provide quantitative methods for rational application of optical heat pulses to examine protein biophysics and manipulate cellular excitability.

Keywords: vestibular, semicircular canals, crista ampullaris, infrared neural stimulation, heat pulse, thermal excitability

NEW & NOTEWORTHY

Go to:

In the present report we demonstrate that electrical excitability in sensory hair cells is thermodynamically sensitive and poised to respond to <1 zJ (10^{-21} J) of thermal energy. We identify key thermosensitive ion channels in hair cells and describe how the Gibbs free energy governing protein conformational state transitions and membrane electrochemistry leads to sensitivity. New experimental and theoretical methods exploit temperature as an independent thermodynamic variable to rapidly manipulate and examine excitability, in the same way voltage is routinely controlled for analogous purposes.

INNER EAR SENSORY HAIR CELLS are exquisitely sensitive to mechanical deflection of specialized microvilli located at their apical surface and are capable of detecting mechanical displacements on the Ångström scale. For this to occur, ion channels associated with mechanoelectrical transduction (MET) and membrane electrical excitability must be poised to open in response to small changes in Gibbs free energy (Arrhenius 1889; Eyring 1935; Hille 1984). Hence, sensitivity comes with the potential for instability. Temperature is the key thermodynamic variable that can be manipulated to reveal enthalpic and entropic terms in the Gibbs free energy. Even relatively small changes in temperature can have profound effects on protein function, intracellular signaling, and membrane excitability. In the ear, thermosensitivity is exemplified by nonsyndromic temperature-sensitive auditory neuropathy, where a mutation in the otoferlin gene causes profound but reversible hearing loss, crippling the inner hair cell synapse when body temperature is high (Marlin et al. 2010; Rodriguez-Ballesteros et al. 2008; Starr et al. 1998; Varga et al. 2006; Wang et al. 2010; Yasunaga et al. 1999). Understanding the basic mechanisms of thermosensitivity of inner ear sensory hair cells and ganglion neurons is essential not only to understand the basis of temperature-sensitive disorders but also for the design and use of thermal stimuli for basic biophysical investigations, hypothermic therapeutic interventions, and infrared (IR) neural stimulation. Toward these goals, we recorded the sensitivity of semicircular canals to heat-pulse stimuli directed to the crista and examined the origins of electrical excitability in response to thermal transients delivered to water by pulses of IR light.

Auditory and vestibular hair cells are very sensitive to pulsed IR stimulation. In the organ of Corti, pulsed IR stimulation evokes robust neural responses in the healthy hearing cochlea that have origins primarily in stimulation of sensory hair cells (Izzo et al. 2006; Schultz et al. 2012; Tan et al. 2015; Thompson et al. 2015; Xie et al. 2015). Part of the response in cochlear hair cells is mechanical and arises from optoacoustic gating of MET channels (Fridberger and Ren 2006; Schultz et al. 2012), whereas the remainder is thermal. Single-unit afferent recordings in the toadfish semicircular canals show a rich repertoire of action potential (AP) responses to pulsed IR light that have origins primarily in thermal action on sensory hair cells (Rajguru et al. 2011). Some postsynaptic afferents responded to IR heat pulse stimulation of the crista with slow excitation, as might be expected based on the classical Hodgkin-Huxley model, where the rate of AP discharge rate increases with temperature (assuming constant current injection). Other semicircular canal afferents, in contrast, responded with rapid inhibition, and yet others were initially inhibited followed by excitation. The most sensitive afferents fired phase-locked APs pulse by pulse with the IR stimulus applied to the crista, consistent with phase-locked transmitter release from hair cells. In both the cochlea and vestibular organs, hair cells are much more sensitive to heat pulses than afferent neurons, with direct stimulation of ganglion neurons typically requiring stimulus levels at least 5 to 10 times higher to change the discharge rate and typically failing to evoke APs on a pulse-by-pulse basis (Rajguru et al. 2011; Thompson et al. 2015). Although hair cell responses to IR heat pulses can be large, the specific molecular mechanisms responsible for thermosensitivity are largely unknown.

A wide array of thermosensitive channels and molecular interactions have been identified previously in other cell types and are expressed in hair cells, the most salient of which are illustrated schematically in Fig. 1*A*. The present work focused on temperature (T) sensitivity of major plasma membrane conduction currents through voltage-gated K^+ channels (Fig. 1*A*, K_V and K_{IR}), large-conductance Ca^{2+}-activated K^+ channels (Fig. 1*A*, BK), and intracellular free Ca^{2+} concentration ($[Ca^{2+}]_i$) signals responsible for BK activation. We also examined plasma membrane capacitive displacement currents (Fig. 1*A*, C_m) driven by the rate of temperature change (dT/dt). Proteins and mechanisms represented by gray labels in Fig. 1*A* are also known to be thermosensitive but were not examined in detail in the present work. Universal among all of these mechanisms is electrical membrane capacitance, which is known to be temperature sensitive in all cells and which, during brief heat pulses, is responsible for a physiologically significant electrical displacement current (Shapiro et al. 2012). During an optical heat pulse, the rate of temperature rise can exceed 500°C/s, rapidly stretching the membrane electrochemical double layers by increasing random thermal motion of ions and thereby effectively injecting net capacitive depolarizing current into the cell (Liu et al. 2014). This same thermoelectric mechanism is present in organelle membranes, including mitochondria and the endoplasmic reticulum, and likely contributes to heat-pulse evoked $[Ca^{2+}]_i$ transients and Ca^{2+}-induced Ca^{2+} release (CICR). In

HeLa cells, for example, evidence suggests that brief heat pulse stimuli modulate $[Ca^{2+}]_i$ transients partially through thermal action on inositol trisphosphate signaling (Fig. 1*A*, IP3R) (Tseeb et al. 2009). In neonatal rat ventricular cardiomyocytes and spiral ganglion neurons, evidence suggests heat pulse stimuli act primarily on Ca^{2+} currents through the mitochondrial Ca^{2+} uniporter (Fig. 1*A*, mCU) and the mitochondrial Na^+/Ca^{2+} exchanger (Fig. 1*A*, mNCX). Heat pulse $[Ca^{2+}]_i$ transients can be reversibly blocked in some cell types by disrupting mCU or mNCX (Dittami et al. 2011; Lumbreras et al. 2014). Calcium- and voltage-independent mechanisms have also been reported. Heat pulses evoke neurotransmitter release in the neuromuscular junction of *Caenorhabditis elegans* (Liu et al. 2014), without requiring Ca^{2+} influx through plasma membrane ion channels (Fig. 1*A*, Afferent, Eff). In addition, virtually all plasma membrane ionic currents are known to be thermosensitive to some extent, with some channels specialized to sense temperature (e.g., Fig. 1*A*, TRP). Among this myriad of temperature-sensitive mechanisms, it is not known which underlie excitation, inhibition, or phase locking in auditory or vestibular ganglion neurons that occur in response to heat pulse stimulation of presynaptic hair cells.

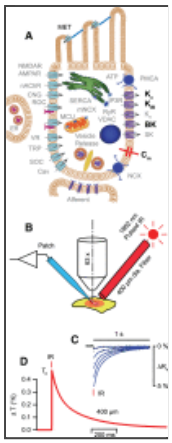

Fig. 1.

IR heat pulse stimulus. *A*: illustration of a type II hair cell showing a subset of temperature-sensitive mechanisms contributing to excitability. Present report addresses heat pulse-evoked membrane currents arising primarily from the delayed K^+ rectifier **...**

In this article, we report electrophysiological data from mammalian semicircular canal afferents and type II hair cells, examining the origins of IR heat pulse excitability. Single-unit afferent recordings in chinchilla demonstrate excitatory, inhibitory, mixed, and phase-locked AP responses to pulsed IR stimulation of the crista in mammals, similar to those reported previously in toadfish (Rajguru et al. 2011). Whole cell voltage-clamp recordings in murine type II hair cells at the resting potential implicate the BK channel as responsible for rapid heat pulse inhibition and a depolarizing capacitive transient plus a prolonged Ca^{2+} influx as contributing to excitation. The relative mix of inhibition vs. excitation varied between hair cells, consistent with diversity of AP responses observed at the postsynaptic level. IR heat-pulse sensitivities of ionic currents reported presently were consistent with temperature-sensitivity predicted by thermodynamic transition-state models of ion channel conformational changes.

METHODS

Go to:

The University of Newcastle Animal Care and Ethics Committee approved all experimental procedures using mice, and the Johns Hopkins Animal Care and Use Committee approved all experimental procedures using chinchilla.

Afferent action potential recordings. Adult female chinchillas ($n = 47$) were used to examine responses of semicircular canal afferents to heat pulse simulation of the presynaptic sensory epithelium in vivo. The surgical procedure and single-unit recording followed methods described previously (Hullar et al. 2005). General inhalation anesthesia of 1–5% isoflurane was maintained during surgery and experimentation, and core body temperature was maintained at 36–38°C. The vestibular nerve was accessed dorsally through the bulla anteromedial of the horizontal and superior canal ampullae, targeting the superior division of the vestibular nerve. Single-unit extracellular recordings used glass micropipettes (20–60 MΩ) filled with 3 M NaCl. Data were bandpass filtered (0.1–5 kHz), amplified (Dagan 2400A; Minneapolis, MN) to span the range of the 16-bit analog-to-digital converter, and

sampled at 10 kHz (CED1401 Spike2; Cambridge Electronic Design, Cambridge, UK). Modulation of the action potential rate to yaw and pitch rotations was used to identify fibers as innervating the horizontal and superior canal, respectively. Fibers that did not respond to rotation were not included in the study. Ex vivo responses of vestibular afferent responses to pulsed IR stimuli were recorded in adult mice (n = 3) following methods reported previously (Lee et al. 2005).

Type II hair cell voltage clamp. Three groups of mice (n = 39; C57/Bl6 or CBA/Caj129 mice, both sexes, 3–5 wk old) were used for ex vivo type II hair cell voltage-clamp experiments following methods described previously (Lim et al. 2011). Mice were anesthetized using ketamine (100 mg/kg ip) and then decapitated. The inner ears were dissected from the head in an ice-cold slurry of glycerol-modified Ringer solution containing (in mM) 26 $NaHCO_3$, 11 glucose, 250 glycerol, 2.5 KCl, 1.2 NaH_2PO_4, 1.2 $MgCl_2$, and 2.4 $CaCl_2$, bubbled with carbogen (95% O_2-5% CO_2). The vestibular triad comprising the utricle, anterior, and horizontal cristae was isolated from the bony labyrinth. The membranous roof was cut from the vestibular triad to form a semi-isolated neuroepithelial preparation. The preparation was then transferred to a bath chamber perfused with Leibovitz's L15 medium (Invitrogen, Mulgrave, VIC, Australia) at ~25°C. Voltage-clamp recordings were made with glass microelectrodes (resistance 3–5 MΩ) and filled with K-gluconate internal solution containing (in mM) 42 KCl, 98 K-gluconate, 4 HEPES, 0.5 EGTA, 1 $MgCl_2$, and 5 NaATP (pH 7.4, osmolality ~295 mmol/kg H_2O). A number of different antagonists were used, including tetraethylammonium (TEA; 10 mM; Sigma Aldrich, Castle Hill, NSW, Australia), 4-aminopyridine (4-AP; 5 mM; Sigma Aldrich), strychnine (1 μM; Sigma Aldrich), tubocurarine (20 μM; Sigma Aldrich), apamin (100 nM; Sigma Aldrich), iberiotoxin (IBTX; 100 nM; Alomone, Jerusalem, Israel), and nifedipine (10 μM; Sigma Aldrich). Voltage- and current-clamp data were collected using a Multiclamp 700A amplifier (Molecular Devices, Sunnyvale, CA). Signals were filtered at 10 kHz, amplified to span the 16-bit range of the analog-to-digital converter, and sampled at 20 kHz (Instrutech ITC1600; HEKA, Lambrecht, Germany). All data were acquired using Axograph X software (J. Clements, Sydney, Australia) and analyzed using custom software written in the Igor Pro environment (Wave Metrics, Lake Oswego, OR).

Heat pulse stimuli. Thermal transients were delivered to hair cells by directing 1,862- to 1,870-nm IR laser light (Capella; Lockheed Martin Aculight, Bothell, WA) to the crista ampullaris using a 400-μm-diameter fiber optic as described previously (Rajguru et al. 2011). For ex vivo voltage-clamp experiments in the mouse labyrinth, the polished tip of the fiber optic was lowered under visual guidance to illuminate the horizontal canal crista with a red pilot light at a distance of ~400 μm (1 fiber diameter) from the epithelium. For in vivo recordings of afferent neural APs in the chinchilla, the fiber optic was positioned under visual guidance to illuminate the superior canal crista at a distance of ~500 μm through an anterolateral fenestration in the bony labyrinth.

Heating by 1,862- to 1,877-nm IR light is achieved primarily through optical absorption by water (Norton and Bowler 2013; Thompson et al. 2013), depositing heat to the tissue and medium (endolymph or perilymph, L15) in a compact pattern in front of the optical fiber. This wavelength is adjacent to a water absorption peak (Curcio and Petty 1951) but far from absorption peaks of proteins and lipid bilayers (Tamm and Tatulian 1997) and thereby delivers heat directly to water and indirectly, by conduction, to proteins and lipids. To estimate the magnitude and kinetics of the thermal transients in the present experiments, we measured the temperature changes in L15 medium in response to the IR stimulus at a distance of ~400 μm in front of the polished fiber optic, consistent with the position of hair cells and afferent spike initiation nodes in the physiological experiments. A glass pipette was positioned at the epithelial site, and the change in the pipette resistance was monitored as a function of time using the same laser power settings and pulse widths used in the experiments. A multisine Fourier method was used to measure the pipette resistance (see *Type II hair cell capacitance measurement*). Calibration curves were obtained for the same pipettes by heating the bath and recording the resistance vs. temperature. For the short pulse widths used in the experiments, the temperature rise was linear in time during the pulse and was fit during relaxation with a double exponential as described below. Thermal transients reported in Figs. 2–9 are estimates based on measurements in the bath at the location of the sensory epithelium in the optical field and at the laser stimulus settings used in the experiments.

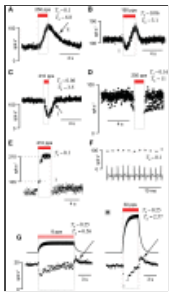

Fig. 2.

Semicircular canal afferent responses to IR pulse trains applied to the crista. *A–F*: example recordings from chinchilla in vivo. *A*: strictly excitatory response using a 250-pps IR stimulus sufficient to raise the temperature ~0.13°C **...**

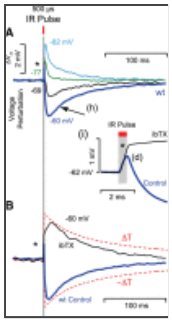

Fig. 9.

Heat pulse depolarization vs. hyperpolarization. *A*: in current clamp from −60 mV, a single IR heat pulse evoked a transient excitatory capacitive depolarization (*d*; *) during the laser pulse in all cells (*inset i*, expanded view), followed by an **...**

Type II hair cell capacitance measurement. Since membrane electrical charge displacement Q_m was dependent on voltage and temperature in the present experiments (2 independent thermodynamic variables), the chain rule of calculus gives the capacitive current as $I_C = C_E(dV_m/dt) + C_T(dT/dt)$ (see Appendix, *Eqs. 2 and 3*), where $C_E = \partial Q_m/\partial V_m$ is the electrical capacitance and $C_T = \partial Q_m/\partial T$ is the thermoelectric capacitance. The thermoelectric capacitance C_T was measured while voltage was held constant ($dV_m/dt = 0$) by recording transient currents evoked by 500-μs-long thermal pulses of constant dT/dt in the time domain. The electrical capacitance C_E was measured while temperature was held constant ($dT/dt = 0$) by using a voltage command consisting of three superimposed sinusoids (~163, 524, and 725 Hz) and extracting capacitance, series resistance, and membrane resistance using Fourier analysis. Both measurements were done in whole cell voltage clamp. Results are reported relative to the unperturbed whole cell capacitance C_m^0 (pF) as the electrical capacitance temperature sensitivity $\gamma_m = (C_E/C_m^0 - 1)/\Delta T$ (°C^{-1}) and the thermoelectric capacitance temperature sensitivity $\lambda_m = C_T/C_m^0$ (mV/°C). Recordings with drift in baseline C_m^0 obscuring γ_m or λ_m were rejected from consideration. Current and voltage signals were filtered at 10 kHz (Axon Instruments) and sampled at 20 kHz with the amplifier gain adjusted to span the 16-bit range of the analog-to-digital converter (HEKA ITC-18). Amplifier whole cell capacitance compensation and series resistance compensation were disabled during capacitance recordings. Fourier components of the current and voltage at each probe frequency were determined using a sliding window spanning five periods of the lowest probe frequency. Frequency components of data in the window were determined using a cosine-weighted Hanning window and a three-component discrete Fourier series computed as a least-squares pseudoinverse of the time domain. The electrical admittance was determined at each probe frequency. The three admittance values were used simultaneously to estimate the effective access resistance, membrane capacitance, and membrane resistance using nonlinear Levenberg-Marquardt optimization (WaveMetrics). Before cells were recorded, frequency-dependent admittances of model cells (physical electrical circuits mimicking passive hair cell properties) were used to determine a calibration transfer function correcting for filtering and delay properties of the recording instrumentation. Proper calibration was validated by recording from model cells with known electrical properties. Ion channels were not blocked during most experiments, so capacitance measurements included contributions from fast voltage-activated ion channels in addition to temperature- and exocytosis-dependent changes.

RESULTS AND DISCUSSION

Go to:

Afferent responses to heat pulse stimulation of the crista. It was shown previously using an in vivo toadfish model that IR heat pulse stimulation of the semicircular canal crista evokes diverse responses in postsynaptic afferent neurons (Rajguru et al. 2011). Results summarized in Fig. 2 demonstrate that the same types of responses are present in mammals. IR heat pulse sensitivity was examined in the

chinchilla in vivo by recording APs in superior and horizontal semicircular canal afferents in response to IR heat pulses applied to ampullae. The thermal stimulus consisted of IR pulse trains delivered to the crista via a 400-μm-diameter fiber located ∼500 μm from the sensory epithelium. Pulse trains were used rather than isolated IR pulses to increase the accumulated temperature and facilitate comparisons to previous data in toadfish (Rajguru et al. 2011). Each individual IR pulse rapidly raised the temperature of the epithelium ∼0.08–0.3°C (T_0; temperature rise per pulse was estimated by calibration in water based on fiber size, pulse width, and laser power; Fig. 1, *C* and *D*, and *Eq. 28*). Pulse trains also generated an accumulated temperature rise of 0.6–11°C (T_Σ; buildup of temperature due to superposition of pulses was estimated by the linear approximation after calibration in water; *Eq. 30*) (Norton and Bowler 2013). IR heat pulse trains were applied at rates of 1–250 pulses/s (pps). Stimuli generating high accumulated temperature (e.g., $T_\Sigma > 3$) would be expected to relax to baseline more slowly due to the larger volume of tissue heated. Afferents in the chinchilla demonstrated a rich diversity of responses consistent with previous data in the toadfish, with representative examples shown in Fig. 2 ($n = 34$). Afferents innervating the stimulated crista responded to the IR pulse trains, whereas afferents innervating alternative organs did not. Some afferents responded strictly with excitation of AP discharge rate (Fig. 2*A*). Recovery of the discharge rate to the prestimulus level in excitatory units followed a time course tracking the temperature relaxation (cf. Figs. 1*D* and 2*A*, arrow), following the accumulated temperature rise T_Σ. A second group of afferents was rapidly inhibited, followed by buildup of a slower excitatory response (Fig. 2*B*). A third group of afferents was strictly inhibited (Fig. 2*C*), and in some cases immediately silenced, on initiation of the pulse train (Fig. 2*D*). A fourth group of afferents responded with APs phase-locked to each IR heat pulse stimulus (Fig. 2, *E* and *F*), with discharge rates either above or below the spontaneous rate. In the example in Fig. 2*E*, the afferent initially responded with one AP every other heat pulse (1:2 ratio) and transitioned to a 1:1 ratio as accumulated temperature increased. Phase locking was observed pulse by pulse in response to thermal transients as low as $T_0 \approx 0.1$°C (Fig. 2*F*), with an average time delay of 2.1 (0.1 SD) ms ($n = 2$).

Inhibition vs. excitation in afferents was observed with nearly equal prevalence in the chinchilla, with 53% of units showing excitation after 1 s of pulse train stimulation and 47% showing inhibition. Excitation, inhibition, and phase locking were strikingly similar to a previous report in toadfish (Rajguru et al. 2011), which is particularly interesting because fish only have type II hair cells and lack type I cells and calyx terminals (Boyle and Highstein 1990; Sans and Highstein 1984). It is also notable that the ambient labyrinth temperature in the toadfish experiments was typically 10°C lower than that in present experiments in chinchilla. In the present study using chinchilla, 45% of units with irregular spontaneous discharge rates were excited after 1 s of stimulation and 55% were inhibited, whereas 52% of regular afferents were excited after 1 s and 48% were inhibited. Given the correlation between regularity and synaptology in the chinchilla (Baird et al. 1988; Lysakowski and Goldberg 1997), results suggest the presynaptic molecular mechanisms responsible for heat pulse sensitivity might be present in both type I and type II hair cells and afferents. Both excitation and inhibition were present with the animal in the same orientation relative to gravity, and in units tested, responses were unchanged when the orientation of the animal relative to gravity was altered. Consistent with a previous report in toadfish (Rajguru et al. 2011), results rule out thermally driven endolymph buoyancy as underlying hair cell activation. IR heat pulse stimuli evoke both excitatory and inhibitory responses in the semicircular canals irrespective of orientation of the optical stimulus relative to hair bundle orientation (Rajguru et al. 2011), which is inconsistent with activation by thermal expansion of the endolymph or optoacoustic activation of MET currents. Although auditory hair cells are sensitive to the photoacoustic component of pulsed optical stimuli (Schultz et al. 2012; Tan et al. 2015; Thompson et al. 2015; Xie et al. 2015), the present work is focused on photothermal mechanisms, which dominate activation of the crista ampullaris in the IR stimulus range used in the present study.

We also examined afferent responses in excised murine semicircular canals to confirm similar responses were present in the ex vivo preparation used for hair cell recordings ($n = 3$ mice). Figure 2, *G* and *H*, provides example responses of a single afferent for heat pulse stimuli at 8 and 30 pps, with power and pulse width providing ∼0.25°C temperature rise per pulse and 0.6–2.6°C accumulated temperature rise (black curves) during the pulse trains. This particular example (Fig. 2, *G* and *H*)

responded with rapid inhibition initiating at the onset of the pulse train that adapted over time, followed by an excitatory rebound that persisted upon cessation of the IR stimulus. Response patterns were consistent with the superposition of a rapid inhibitory component that adapted faster than thermal transient plus a slower excitatory component that tracked the thermal transient. Similar to responses in the toadfish (Rajguru et al. 2011) and chinchilla (present report), the inhibitory component in mouse developed and decayed more rapidly than the excitatory component, in some units leaving the excitatory component as dominant during recovery as the tissue cooled to the prestimulus condition (Fig. 2, *G* and *H*, arrows). Adjusting the relative mix of the rapid inhibitory component and the slower excitatory component qualitatively explains the broad diversity of afferent responses observed in all three species tested.

Heat pulse modulation of action potential generation. We examined the kinetics of IR heat pulse-evoked APs to determine the contribution of thermosensitivity of afferent spike generation on observed responses. Because the first heminode of Ranvier is located just below hair cells (Lysakowski et al. 2011) and was in the optical path of the IR stimulus in the present experiments, it is likely that part of the excitatory response reported here was due to direct thermal activation of afferent spike generators. To gain some insight into feasibility of this idea, we recorded AP kinetics in mouse afferents and compared results to simulated AP kinetics using a single-compartment Hodgkin-Huxley (HH) model with temperature-dependent channel rate constants ($Q_{10} = 3$; Hodgkin and Huxley 1952; Hodgkin and Katz 1949; Huxley 1959; Weiss 1996). Heat pulse-driven thermoelectric capacitive currents were also included in the simulations (see Appendix) (Shapiro et al. 2012). The HH model was biased by using a constant current injection to poise the neuron near the threshold of AP generation and then subjecting it to IR heat pulse transients (thermal stimuli followed kinetics in Fig. 1*D*). Simulated voltage responses are shown in Fig. 3*A* for 500-μs IR heat pulse stimuli with the laser power adjusted to generate a temperature rise from 0.25°C (present experiments) up to 2.5°C. For a single IR heat pulse to evoke an AP in the model, a stimulus strength approximately sixfold higher than that used in the present experiments was required. As noted below, AP generation in murine semicircular canals has a $Q_{10} \approx 2$, which is lower than that of the squid giant axon and much too low for direct phase-locked AP generation by a 0.25°C thermal transient. Current leakage down the axon would be expected to further reduce sensitivity relative to the space-clamped HH model simulated here, suggesting that direct activation of afferent APs was highly unlikely. When pulsed IR did evoke phase-locked APs in the present experiments and in a previous study (Rajguru et al. 2011), there was always a delay between the IR heat pulse and the AP that was inconsistent with direct heat pulse activation of afferents (e.g., Fig. 3*A*). The HH model describing direct activation of afferents cannot account for the delay and requires at least sixfold higher temperature transients to evoke phase-locked AP, suggesting phase-locked APs had origins in heat pulse activation of hair cells. Results are consistent with a previous report where direct IR heat pulse stimulation of semicircular canal afferent cell bodies failed to evoke phase-locked APs, failed to evoke inhibitory responses, and only modestly increased the asynchronous AP discharge rate (Rajguru et al. 2011).

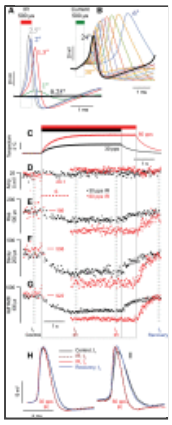

Fig. 3.

Temperature-dependent AP kinetics. *A*: HH simulations for the squid giant axon using $Q_{10} = 3$ (Hodgkin and Katz 1949; Weiss 1996) in response to a single 500-μs-long IR heat pulse. Simulations include thermoelectric capacitive currents. APs were **...**

Afferents were sometimes driven to complete but reversible silence by IR pulse trains, which raised the possibility that thermal block of AP generation might have contributed (Hodgkin and Katz 1949). To

explore this idea, we simulated APs in the HH model of the squid giant axon at temperatures from 6 to 38°C in response to current pulses. As illustrated in Fig. 3*B*, simulated APs became faster and smaller with increased temperature and eventually failed to fire due to thermal block (Hodgkin and Katz 1949; Weiss 1996), a phenomenon that occurs at higher temperatures in mammals (Duke et al. 2013). To determine if thermal block occurred in the present experiments, we monitored AP amplitude and kinetics during IR pulse trains at 30 pps (Fig. 3, *C*–*G*, black) and 60 pps (Fig. 3, *C*–*G*, red), generating ~2.6 and 5.2°C accumulated temperature increases, respectively. APs failed to show the signature reduction in amplitude required for thermal block (Fig. 3*D*), providing further evidence that inhibition was due to IR action on hair cells leading to a reduction in transmitter release and not due to direct thermal block of AP generation.

APs increased kinetics with temperature, demonstrating that the spike initiation site was located in the IR laser light path, at the first heminode just below the sensory epithelium. Using IR pulse trains (Fig. 3*C*), we measured changes in the AP rise time (Fig. 3*E*), decay time (Fig. 3*F*), and half width (Fig. 3*G*) in murine semicircular canal afferents. The average temperature sensitivity of AP kinetics was estimated from these data to be $Q_{10} = 2.18$ (0.47 SD). The excitatory change in AP kinetics shows that IR action on vestibular AP generation is strictly excitatory and would be expected to lead to modest increases in AP discharge rate with accumulated temperature rise. Inserting $Q_{10} = 2.2$ into the HH model and evoking spike trains at 100 spikes/s using current injection predicted an increase in firing rate of ~11 spikes/s per °C increase in accumulated temperature. This increase in firing rate is slow and tracks the increase in accumulated temperature, but it is the result of increases in the fast kinetics of ion channels and AP generation. The HH-predicted firing rate increase was asynchronous, in that individual IR heat pulses did not evoke phase-locked APs. These simulations provide further evidence that thermal sensitivity of afferent AP generation cannot explain inhibition or phase locking of APs or inhibition of AP discharge rate, implying the origins of these key events is in sensory hair cells.

On the basis of recordings in other cell types, we hypothesized that hair cells would respond to heat pulses with transient capacitive currents (Shapiro et al. 2012), thermal opening of ion channels (Latorre et al. 2007; Liu et al. 2014; Yang and Zheng 2014), $[Ca^{2+}]_i$ transients (Dittami et al. 2011; Lumbreras et al. 2014; Tseeb et al. 2009), and potentially direct modulation of neurotransmitter release (Liu et al. 2014). Below, we present electrophysiological data quantifying the thermoelectric component of type II hair cell hair cell excitability.

Heat pulse modulation of membrane capacitive currents. To determine the role of thermosensitive electrical capacitance on heat pulse excitability, we recorded capacitance modulation in murine type II hair cells using whole cell voltage clamp before and after application of a 500-μs heat pulse ($n = 16$). Figure 4*A* shows results for a typical cell in response to a single heat pulse that raised the temperature ~0.25°C and subsequently cooled passively to the prepulse temperature. Capacitance (gray curves) increased rapidly during the pulse and recovered to baseline following the temperature transient, consistent with previous recordings in outer hair cells and model systems (Okunade and Santos-Sacchi 2013; Shapiro et al. 2012). Smooth curves show the temperature (*Eq. 25*), scaled to match the peak magnitude of the capacitance change recorded at three different holding potentials ($\Delta T \approx 0.25$°C in all 3 cases). Correspondence between the curves and whole cell recordings shows the capacitance closely tracked the local temperature in all cases but varied in magnitude based on the holding potential. For pulse trains, individual heat pulses superimposed to generate an accumulated temperature rise and an accumulated increase in capacitance (Fig. 4*B*, dashed gray curve) (Liu et al. 2014; Norton and Bowler 2013). The solid black curve is a superposition of temperature transients (*Eq. 30*) with the overall magnitude scaled to match the capacitance transient. Correspondence between the transient capacitive change and temperature is striking and demonstrates that membrane capacitance linearly tracks temperature, at least for heat pulse magnitudes used in the present study. The magnitude of the heat pulse-evoked capacitance change increased as the cell was hyperpolarized (Fig. 4*C*; $n = 17$), reaching a peak near −120 mV and a minimum near −30 mV. Ion channels were not blocked during capacitance recordings, so voltage-gated channels with kinetics faster than the interrogation Nyquist frequency would be expected to contribute to C_m. To account for this, the change in capacitance ΔC_m evoked by a change in temperature ΔT, and normalized to the baseline capacitance C_m^0, was quantified by γ_m (Fig. 4*C*). Voltage and temperature dependence of the membrane double layer would predict γ_m (*Eq. 3*)

to have the shape of an inverted bell curve (Chapman 1913; Gouy 1909; Stern 1924), motivating our use of *Eq. 27* (solid black curve) to describe voltage dependence. At the resting membrane potential, the increase in capacitance was ~3% per °C increase in temperature. Temperature-dependent changes in specific membrane capacitance were large (on the order of 100 fF for a 0.25°C 500-μs heat pulse) and in the present experiments masked increases in capacitance associated with exocytotic events increasing membrane surface area (on the order of 1 fF for a 1-ms depolarization).

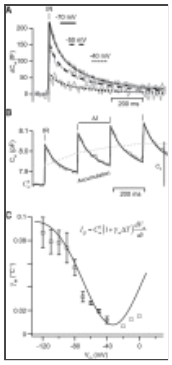

Fig. 4.
Temperature-dependent electrical capacitance. *A*: a single IR heat pulse evoked a rapid increase in whole cell capacitance (gray) during the laser stimulus that slowly returned to the prepulse level as the temperature relaxed to baseline. Smooth curves **...**

We quantified the thermoelectric capacitance coefficient λ_m (*Eq. 3*) by measuring the current during the laser pulse in whole cell voltage clamp. Figure 5*A* shows that during the heat pulse, the current consisted of a rectangular step (proportional to d*T*/d*t*) plus a linear component (proportional to *T*). The rectangular step is the capacitive thermoelectric current, whereas the linear part arises from the temperature-dependent conductance change (see METHODS and *Eqs. 1–4*). After major K^+ ion channels were blocked with TEA and 4-AP, the capacitive thermoelectric current was linear with voltage (Fig. 5*B*, black line, $n = 3$), consistent with previous reports (Carvalho-de-Souza et al. 2015; Shapiro et al. 2012). When channels were not blocked, the effective capacitive thermoelectric current became nonlinear and reversed sign as the cell was depolarized (Fig. 5*B*, red curve, $n = 13$) (Liu et al. 2014; Okunade and Santos-Sacchi 2013). At the resting membrane potential near −60 mV, thermoelectric excitability was $\lambda_m \approx -9$ mV/°C in both cases. This means that a single heat pulse delivered with a duration much shorter than the membrane time constant would depolarize the cell by 9 mV for each 1°C temperature rise (*Eq. 5*). Heat pulse stimuli used in the present experiments were on the order of 0.25°C for a 500-μs pulse, corresponding to a capacitive depolarization of about 2 mV. The duration of the capacitive current is only as long as the IR heat pulse, 500 μs for data shown from hair cells in the present report. At the resting membrane potential, this depolarizing capacitive current was accompanied by a hyperpolarizing conduction current as described below.

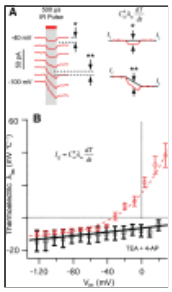

Fig. 5.
Voltage-dependent thermoelectric capacitance. *A*: the rapid temperature rise during the laser heat pulse evoked a voltage-dependent thermoelectric current, $C_m{}^0\gamma_m(dT/dt)$, superimposed on top of the temperature-dependent conduction current, I_G (indicated **...**

Heat pulse modulation of membrane conduction currents. Unlike the change in capacitance (Fig. 4), ΔI did not decay in step with the temperature transient, but instead decayed with a time constant approximately fourfold faster. The time course was measured by application of individual IR heat pulses during a voltage-clamp ladder protocol. Recordings were also performed in current clamp after identification of major heat pulse-sensitive currents (presented in Fig. 9). Starting from a holding potential of −60 mV, a ladder of 300-ms voltage-clamp commands from −120 to +20 mV was applied in 10-mV increments, followed by a 100-ms hold at −30 mV. An IR heat-pulse was superimposed in the center of the voltage command to determine voltage dependence and kinetics of the heat pulse-evoked current. Example recordings in the control condition and the heat pulse condition are shown in

Fig. 6, *A* and *B*. Subtracting the control condition from the heat pulse condition revealed the heat pulse-evoked current (Fig. 6*C*, Δ*I*, black curves). In the control condition, the large outward current at depolarized voltages arose primarily from voltage-activated delayed rectifier K^+ channels (Rusch et al. 1998; Rutherford and Roberts 2009). These channels open in response to voltage with time constants on the order of 1–10 ms, with the faster opening occurring at more depolarized levels. The heat pulse-evoked Δ*I* was much faster than voltage-evoked channel opening, rising to its peak value in step with temperature (<1 ms with no detectable delay within instrumentation limits). Decay of the heat pulse current was much faster than relaxation of the temperature, demonstrating that the current was not a simple reflection of temperature (as would be the case for temperature-dependent conductance of ionic solutions, for example). Instead, the rapid decay reflects kinetics of thermosensitive ion channel conformational changes.

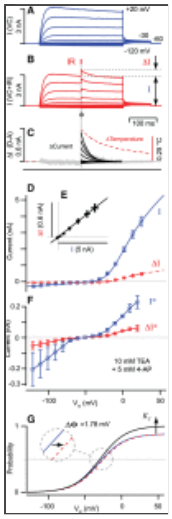

Fig. 6.

Heat pulse-evoked conduction currents. Whole cell conduction currents were recorded in response to 300-ms voltage steps in 10-mV increments in the control condition (*A*) and with a 0.25°C heat pulse applied in the center of the voltage command **...**

Although kinetics of voltage activation and thermal activation differed dramatically, the equilibrium currents had almost identical voltage dependence, suggesting the currents were likely to have been carried by the same ion channels. Figure 6*D* provides whole cell current-voltage (*I-V*) relations for voltage stimuli (blue; *I* in Fig. 6*B*) and for heat pulse stimuli (red; Δ*I* in Fig. 6*B*). Error bars show 1 SD of the mean across cells ($n = 13$). On average, the membrane resistance at −60 mV was 489 MΩ and the access resistance was <8 MΩ. The temperature-dependent change in electrode resistance during the laser heat pulse was <2 MΩ/°C. Hence, the error in voltage due to thermal reduction in series resistance was small in present experiments and therefore ignored. Plotting Δ*I* vs. *I* (Fig. 6*E*) revealed a strong linear relationship between the heat pulse- and voltage-evoked currents ($\Delta I = 0.137 \cdot I$, $R^2 = 0.98$), and scaling Δ*I* caused the two curves in Fig. 6*D* to overlap for both negative and positive currents. Application of TEA and 4-AP to block K^+ channels greatly reduced both the voltage-evoked *I* and the heat pulse-evoked Δ*I* (Fig. 6*F*) but did not change the linear relationship between the two. This suggests that the primary action of the heat pulse was to rapidly increase the open probability of whatever channels were already in the activated state. To further test this, we fit the *I-V* curves in Fig. 6*D* with a simple leak current plus a Boltzmann curve to determine how the whole cell open probability might have changed with the application of a heat pulse (solid blue and dashed red curves). The open probability curves arising from this analysis are shown in Fig. 6*G* before the heat pulse (solid blue) and after the heat pulse (solid black). The primary consequence of the heat pulse was to increase the peak open probability by 14% (Fig. 6*G*, up arrow). For comparison, the temperature-dependent change in conductance of the ionic milieu itself was <1% for the same magnitude thermal pulse. The increase in peak open probability was accompanied by a slight rightward shift in the activation potential of 1.78 mV (Fig. 6*G*, right arrow), revealed by scaling the peak probability of the postpulse condition to match the prepulse condition (dashed red = scaled solid black). The standard deviation of the half activation potential was 0.85 mV, and the standard deviation of the peak change in current was 0.22 nA, rendering both the change in peak open probability and the shift in activation potential statistically significant ($n = 15$; $P < 0.02$). At depolarized voltages, temperature sensitivity was dominated by voltage-sensitive K^+ channels.

Simulation of heat pulse modulation of a delayed rectifier K^+ channel. To confirm thermodynamic consistency, we simulated IR heat pulse responses of delayed rectifier K^+ channels and compared kinetics with those of currents recorded from hair cells. Thermodynamic models capable of describing both voltage and thermal activation require at least three conformational states (Latorre et al. 2007; Liu et al. 2003; Sigg et al. 1999; Yang and Gruebele 2003), and for simplicity, we used a minimum three-state model to interpret the present data (see Appendix). Simulated currents are shown in Fig. 7 in response to the same voltage and IR heat pulse stimuli used in Fig. 6. The three-state thermodynamic model captures the dramatic difference in kinetics between voltage activation and thermal activation (Fig. 7*A*). The model simulates whole cell currents as well as single-channel currents (Fig. 7*B*). Thermal activation (Fig. 7*C*) was isolated by subtracting activation curves (Fig. 7*A*) simulated with and without the IR heat pulse applied. The reason the thermally evoked current decays faster than the temperature in the model is due primarily to the number of independent subunits that must change conformation for the channel to open or close. The heat pulse current ΔI has two parts, one arising from temperature sensitivity of voltage-dependent activation (Fig. 7*D*, arising from rate constants k_{12} and k_{21}) and the other from temperature sensitivity of single-channel opening (Fig. 7*E*, arising from rate constants k_{23} and k_{32}). Simulated *I-V* curves (Fig. 7, *F* and *G*) compare favorably with experimental data (Fig. 6, *D* and *E*). The increase in the peak open probability and rightward shift of the activation potential (Fig. 7*H*) are also similar to experimental observations (Fig. 6*G*) and arise naturally in the model from the change in enthalpy between open, activated, and closed states (Yang and Zheng 2014). Although delayed rectifier and inward rectifier K^+ channels dominated the heat pulse responses at depolarized and hyperpolarized potentials, additional channels contributed at the resting potential and were responsible for the diversity of heat pulse excitation vs. inhibition in hair cells.

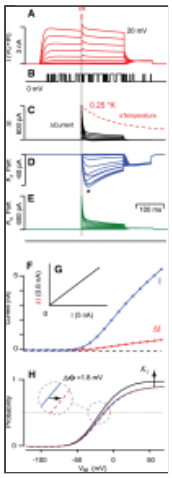

Fig. 7.
Thermodynamic simulation of whole cell delayed rectifier K_{DR} current. *A*: simulated currents in response to voltage steps from −120 to 20 mV with IR heat pulses superimposed during the pulse (cf. Fig. 6*B*). *B*: single-channel simulation showing an **...**

Diversity of heat pulse inhibition vs. excitation. At a −60 mV holding potential, 67% of cells responded to an IR heat pulse with a net inhibitory current, whereas 33% responded with a net excitatory current (Fig. 8*A*, $n = 21$). The sigmoidal transition from inhibition to excitation with voltage arises because the net heat pulse reversal potential differs between individual cells (range ~25 mV). Hence, the array of ion channels contributing to the net heat pulse current varies between cells and likely underlies at least part of the diversity present in responses of afferents to IR stimulation of the crista (Fig. 2). The fraction of cells excited vs. inhibited at a given voltage presumably reflects the relative levels of expression of thermosensitive plasma membrane ion channels in specific cells, as well as differences in heat pulse-triggered intracellular Ca^{2+} signaling (Dittami et al. 2011; Tseeb et al. 2009). TEA plus 4-AP had little effect on the IR-evoked current at the resting potential but large effects at depolarized and hyperpolarized potentials (Fig. 6). Results implicate both K^+ and Ca^{2+} as major players, with K^+ currents dominating at highly depolarized and hyperpolarized membrane potentials and Ca^{2+} likely dominating near the K^+ reversal potential.

Fig. 8.
Heat pulse excitation vs. inhibition. *A*: when depolarized above −20 mV, all hair cells were inhibited by each IR heat pulse, and

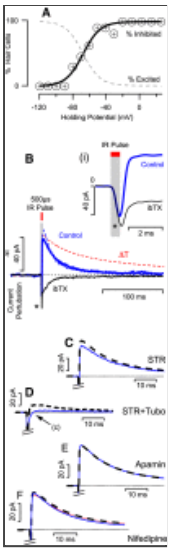

when hyperpolarized below −90 mV, all cells were excited (*n* = 21). Equal numbers of cells were inhibited vs. **...**

Large-conductance Ca^{2+}-activated K^+ channels underlie inhibition. To dissect the potential contributions of specific ion channels to heat pulse excitability at the resting potential, we examined responses in the presence of several pharmacological agents. IR stimulus-triggered averaging over ~40 presentations was used to improve signal to noise for each cell, and final curves show averages across cells. In the control condition, a single heat pulse always evoked a transient excitatory capacitive current (Fig. 8, *B* and *inset*; asterisk indicates laser pulse, ~40 pA) during the IR pulse. In a majority of cells, inhibitory cells, the capacitive current was immediately followed by a prolonged outward conduction current (Fig. 8, *B* and *inset*, blue curve, ~40 pA). The inhibitory current decayed with a time constant of ~24 ms. Application of 100 nM IBTX, a selective blocker of large-conductance Ca^{2+}-activated (BK) channels (Galvez et al. 1990), eliminated the inhibitory current and unmasked an excitatory component (Fig. 8, *B* and *inset*, black curves, average of *n* = 6 cells). The control condition was largely recovered after washout (Fig. 8*B*, blue dashed curve). The excitatory component consisted of the capacitive transient that grew linearly during the IR pulse (Fig. 8*B*, *inset*), plus a net excitatory conduction current. The current unmasked by IBTX was always inward at the voltages tested and grew with membrane hyperpolarization, consistent with thermal activation of plasma membrane Ca^{2+} channels. The heat pulse-evoked IBTX-sensitive inhibitory current peaked at a latency of ~2.6 ms (8.1-ms latency to peak voltage in current clamp), and the putative Ca^{2+} current peaked at a latency of ~3.3 ms (11.6-ms latency to peak voltage in current clamp). On the basis of previous data in the neuromuscular junction, one might expect heat pulses to release ACh from efferent terminals (Liu et al. 2014). Application of 1 μM strychnine and/or 20 μM tubocurarine (average of *n* = 5 cells), blockers of efferent ACh receptors in these cells, led to a net increase in the evoked current (Fig. 8, *C* and *D*, black dashed curves, ~5 pA re: controls, solid blue curves). The net increase in current is consistent with a decrease in heat pulse-evoked Ca^{2+} influx. Apamin (100 nM) did not reveal a detectable change. Also, 10 μM nifedipine (average of *n* = 4 cells) had little effect on whole cell heat pulse-evoked currents (Fig. 8*F*), suggesting that thermal sensitivity of L-type Ca^{2+} currents, presumably present to some extent, did not contribute significantly to heat pulse activation of the IBTX-sensitive current. Together, these data indicate that plasma membrane Ca^{2+} influx might not have been required for activation of the IBTX-sensitive heat pulse current. Although present data (Fig. 8, *C* and *D*) suggest that ACh receptors might have been activated by each heat pulse, Ca^{2+} influx apparently did not lead to SK channel activation since apamin did not change the response (Fig. 8*E*, black dashed curve; control condition, solid blue curve). The hyperpolarizing component in the control condition was less pronounced or absent in some cells (e.g., Fig. 8*D*, blue curve), presumably reflecting diversity of expression levels of the thermoactivation of BK channels.

Current-clamp recordings confirmed the blocking action of IBTX on heat pulse-evoked inhibition. Under control conditions near −60 mV, cells from wild-type mice responded to a 500-μs 0.25°C heat pulse initially with a depolarizing transient [Fig. 9*A*, *d* and *inset i*), as expected from the thermoelectric capacitance of these cells (see Fig. 5*B*). This depolarization was immediately followed by a prolonged hyperpolarization (Fig. 9*A, h*). The inhibitory component was eliminated because the cell was

hyperpolarized beyond the K^+ reversal potential (Fig. 9*A*, blue, −60 mV; black, −69 mV; green, −77 mV; light blue, −82 mV), demonstrating the current was carried primarily by K^+. Consistent with voltage-clamp results (Fig. 8*B*), application of 100 nM IBTX eliminated the hyperpolarization (Fig. 9*B*, blue, control condition vs. black, IBTX) and unmasked a depolarizing component (Fig. 9*B*, black, IBTX). Recovery to baseline was slower under current clamp vs. voltage clamp (46.8 vs. 24.6 ms) but remained faster than decay of the thermal transient ΔT. An expanded timescale (Fig. 9*B*, asterisk in *inset i*) revealed the thermoelectric capacitive depolarization growing during the IR pulse and subsequent conduction current hyperpolarization in the absence of IBTX. The prolonged depolarizing current revealed in the presence of IBTX was putatively due to IR heat pulse-evoked Ca^{2+} influx as noted above (Figs. 6 and 8).

Present data implicate the BK channel as responsible for heat pulse-evoked inhibition. Evidence from outer hair cells located in the basal region of the cochlea (Rohmann et al. 2015; Wersinger et al. 2010) demonstrate a role for BK channels in efferent modulation of hair cell sensitivity. In guinea pig type II vestibular hair cells (Kong et al. 2005, 2007), bath application of ACh opens BK channels, but kinetics was quite slow in those experiments, indicating BK might have been activated indirectly through intracellular CICR (Saito 1980; Wersinger and Fuchs 2011). It has been shown previously using heat pulse stimuli similar to those used in the present study that intracellular Ca^{2+} transients are robustly evoked in multiple cell types without requiring plasma membrane Ca^{2+} influx (Dittami et al. 2011; Lumbreras et al. 2014; Tseeb et al. 2009). It is highly likely that $[Ca^{2+}]_i$ transients were also evoked in the present experiments and that BK activation might have been influenced by colocalization with intracellular stores and heat pulse release from intracellular stores (Saito 1980; Wersinger and Fuchs 2011).

Type II hair cell responses in the presence of IBTX implicate Ca^{2+} influx is likely to be the dominant heat pulse-evoked plasma membrane current. Thermoelectric capacitive depolarization was always present but in smaller magnitude than the heat pulse-evoked conduction currents (Figs. 8 and 9). Present data are not sufficient to determine if heat pulse-evoked Ca^{2+} influx via L-type Ca^{2+} channel contributed to vesicular release and IR phase-locked APs. Responses with nifedipine in the bath failed to reduce the net IR heat pulse-evoked current, so if L-type Ca^{2+} channels were involved, the currents must have been small and obscured by larger heat pulse-evoked currents in our whole cell recordings. It was suggested previously that vesicular release from hair cells might be triggered by IR heat pulse-evoked Ca^{2+} release from intracellular stores (Rajguru et al. 2011). Present results imply that $[Ca^{2+}]_i$ transients were evoked by heat pulses, but the short ~2-ms delay between the IR pulse and phase-locked APs in the present experiments is fast relative to expected diffusion times and suggests that $[Ca^{2+}]_i$ transients might have been augmented by another mechanism. An alternative hypothesis is direct heat pulse excitation of the synaptic release complex. It is well established in conventional synapses that hypertonic solutions evoke synaptic release without requiring intracellular Ca^{2+} increases (Rosenmund and Stevens 1996), putatively due to increased susceptibility to release by Brownian motion (Jahn and Fasshauer 2012). Hypertonic solutions also evoke release from type II vestibular hair cells, suggesting that, like other synapses, the synaptic machinery is likely poised for release and sensitive to Brownian motion. Therefore, it is reasonable to expect synaptic vesicle release from hair cells to be temperature sensitive, even in the absence of changes in intracellular Ca^{2+}.

Summary and conclusion. It has been shown previously that optical heat pulse stimulation of the cochlea can lead to transduction through photoacoustic mechanical activation of hair cell MET currents (Schultz et al. 2012; Tan et al. 2015; Thompson et al. 2015; Xie et al. 2015). Unfortunately, hair cell photoacoustic sensitivity is usually completely absent in cases of severe auditory and vestibular loss, rendering the photoacoustic component of the response to optical stimulation unavailable as a means to restore cochlear or vestibular sensation. In the present work we examined another key component of IR optical stimulation, photothermal activation, which modulates excitability of hair cells and inner ear ganglion neurons through direct thermal action on key proteins and lipids, without requiring mechanotransduction.

Whole cell voltage-clamp recordings in type II vestibular hair cells revealed exquisite pulse-by-pulse sensitivity to thermal transients. Consistent with previous reports in other cell types (Liu et al. 2014;

Shapiro et al. 2012), murine hair cells responded to each 500-μs heat pulse with a thermoelectric capacitive depolarization of ~9 mV/C°, providing the entire cell was stimulated with optical space clamp. This magnitude of depolarization is sufficient to gate L-type voltage-activated Ca^{2+} channels and likely contributed to synchronous pulse-by-pulse neurotransmitter release from hair cells and AP phase locking observed in afferent neurons. Capacitive transients arise from temperature-driven charge displacement in the plasma membrane electrochemical double layer and in membrane-associated proteins. It is an electrical displacement current, which modulates the membrane potential only if the laser pulse depositing the heat is much shorter than the membrane time constant. Sensory hair cells are uniquely sensitive to heat pulse capacitive currents, because hair cells are specialized to rapidly release synaptic vesicles phase-locked to small graded changes in membrane potential at auditory frequencies. Unlike neurons, large APs are not required for synchronous transmitter release from inner ear hair cells.

A majority of type II vestibular hair cells also responded to each IR heat pulse with an inhibitory conduction current, which immediately followed the excitatory capacitive transient. Hyperpolarization reduces transmitter release from hair cells, and the resulting inhibitory current is sufficient to explain heat pulse inhibition of AP discharge rate observed in a subset of postsynaptic vestibular afferent neurons. The inhibitory current was blocked by IBTX, implicating large-conductance Ca^{2+}-activated K^+ (BK) channels as responsible for heat pulse inhibition. Application of IBTX further unmasked an inward conduction current, consistent with heat pulse activation of plasma membrane Ca^{2+} channels. However, application of nifedipine, apamin, strychnine, and tubocurarine failed to substantially alter the IBTX-sensitive current, indicating that BK channels might have been activated at least in part by heat pulse-evoked Ca^{2+} release from intracellular stores rather than exclusively from Ca^{2+} influx. Heat pulse-evoked intracellular Ca^{2+} transients involving multiple mechanisms have been documented previously in other cell types, and similar mechanisms would be expected to lead to intracellular transients in hair cells (Dittami et al. 2011; Lumbreras et al. 2014; Tseeb et al. 2009).

In the present experiments, heat pulses were delivered through IR absorption by water, thus activating diverse and potentially offsetting mechanisms simultaneously. Core body temperature also acts on multiple mechanisms simultaneously. Whether or not the inner ear utilizes offsetting thermosensitivity to its advantage is unknown, but one unavoidable fact is that the inhibitory action of temperature on hair cell BK channels would partially offset the excitatory action of temperature on ion channels and afferent AP generation. The combined effect would reduce the sensitivity of auditory and vestibular afferent signals to changes in temperature. This could be particularly important for animals that operate over a broad range of core body temperatures. Poikilotherms provide extreme examples that must implement temperature-compensating mechanisms in the inner ear to maintain hearing and balance. Analogous temperature-compensating mechanisms are at play in mammals, as well. Regularly discharging semicircular canal afferents in mice show very little, if any, change in sensitivity to angular head movements with a 5°C change in core body temperature (Park et al. 2010), insensitivity that would be advantageous to maintain a proper compensatory vestibulo-ocular reflex with changes in temperature. Irregularly discharging afferents in mouse are more sensitive to changes in temperature (Park et al. 2010), but this same correlation was not present in toadfish (Rajguru et al. 2011), perhaps reflecting differences in the range of core body temperatures experienced by these diverse species. Delivering heat pulses to cells through water absorption carries implicit nonspecificity, motivating development of alternative targeted approaches.

Results also show that AP firing in vestibular ganglion neurons is increased by accumulated temperature. Although endogenous thermosensitivity in inner ear ganglion neurons is much less than in hair cells and appears not to evoke APs on a pulse-by-pulse basis, sensitivity is sufficient to modulate AP rates using optical thermal stimuli. Temperature increases AP ion channel kinetics at the initial heminode of Ranvier with $Q_{10} \approx 2$, thereby leading to modest asynchronous increases in AP discharge rate as the tissue temperature rises. This ion channel-dependent increase in discharge rate is driven by the accumulated temperature rise, ΔT, and is largely independent of the rate of thermal deposition, dT/dt. In addition to asynchronous thermal excitation, brief IR heat pulses with durations shorter than the membrane time constant evoke capacitive currents capable of depolarizing neurons on a pulse-by-pulse basis. Unfortunately, optical space clamp cannot be achieved in vestibular or spiral ganglion

neurons in vivo. Lack of optical space clamp reduces the capacitive current and introduces an unavoidable leak conduction current down the axon. Based on simulations, lack of optical space clamp would be expected to reduce the capacitive depolarization to ~2 mV/C° in ganglion neurons, ~4 times less than we recorded in hair cells. This level of pulse-by-pulse depolarization would be expected to trigger APs for neurons poised near threshold, but in deaf animals the capacitive transient is likely insufficient because ganglion neurons generally do not have synaptic inputs from hair cells and are not poised to fire. Results indicate IR evokes APs in spiral ganglion neurons of deaf animals (Tan et al. 2015) primarily through the Q_{10} of AP generation (shown in this work), which is augmented by additional temperature sensitive channels (Albert et al. 2012). This interpretation is consistent with single-unit recordings during heat pulse stimulation of vestibular ganglion neurons, which exhibit modest increases in discharge rate tracking accumulated temperature rise but do not phase lock APs to individual IR pulses (Rajguru et al. 2011). Nevertheless, it remains possible that heat pulse capacitive transients could evoke phase-locked APs in inner ear ganglion neurons if the cells could be depolarized to rest near the threshold of firing before application of the IR heat pulse.

Hair cells, in contrast, maintain tonic transmitter release and are poised to modulate transmitter release in response to IR heat pulses. Because of this sensitivity, hair cells could be a relevant neuromodulatory target in some conditions. For example, bilateral gentamicin ototoxicity, a leading iatrogenic cause of severe vestibular deficiency in humans (Minor 1998; Sun et al. 2014, 2015), involves selective loss of type I hair cells and potential loss of MET in type II hair cells. Synaptic function in remaining hair cells likely remains intact (Sun et al. 2015). IR heat pulse stimulation has potential as a neuromodulatory stimulus in this setting through action on synaptic transmission from hair cells. The stimulus might also be useful in genetic diseases that selectively interfere with hair cell MET channels (e.g., TMC1, TMC2, PCDH15, and genes involved in Usher syndrome). If the only change in hair cells is the loss of MET, IR heat pulse stimuli would be expected to evoke synchronous phase-locked transmitter release in a subset of hair cells, a BK-mediated asynchronous reduction in a second subset of cells, and a mix of the two in a third subset of cells.

The present work introduces new methods to apply heat pulse stimuli and to interpret responses in a consistent thermodynamic framework. Specifically, we describe the thermoelectric capacitance (*Eq. 2*) and show how it differs from the well-known electrical capacitance. We also derive a simple relationship for membrane depolarization that occurs in response to short optical heat pulses (*Eq. 5*), Depolarization occurs because of the thermoelectric capacitance as well thermally driven ionic conduction currents. We further demonstrate how rapid temperature-driven changes in conduction currents arise naturally in transition state theory (Eyring 1935) from the Gibbs free energy governing protein conformational changes (*Eqs. 17–19*). These same thermodynamic principles apply to organelle membranes, intracellular signaling, and key protein complexes such as the synaptic release machinery. The methods used in the present work highlight temperature as an independent thermodynamic variable that can be rapidly controlled to manipulate protein conformational states and molecular interactions, in the same way that voltage is an independent thermodynamic variable that is routinely controlled to manipulate voltage-sensitive ion channels. Virtually all channels and biomolecular interactions depend on temperature. Command of temperature is a powerful tool that can be used to examine the fundamental energetics underlying protein function in health and disease, and to explore therapeutic interventions that alter protein function through action on the Gibbs free energy.

Given the power of heat pulses to manipulate reaction kinetics and protein conformations, it is interesting to speculate how one might make more effective use of transient thermal stimuli in the future. IR heat pulses have direct applications for neural modulation and as a screen for genetic mutations or drugs influencing protein function. Current optical technologies can focus heat pulses to individual cells, but targeting heat pulses to specific proteins or membrane compartments would dramatically increase potential uses. Nanoparticles targeted to specific cells, proteins, or lipids and tuned to heat when excited by specific wavelengths can be used to command temperature on a molecular scale, thereby providing a means to manipulate excitability and signaling from the ground up. Targeting can be chemically driven and/or enhanced by genetic manipulation to express targets of functionalized particles. Enabling targeted nanotechnologies capable of delivering both hot and cold pulses are beginning to emerge, providing a new set of molecular thermodynamic tools for use as

probes, stimuli, and therapeutics (Carvalho-de-Souza et al. 2015; Mitsunaga et al. 2011; Paviolo et al. 2014; Roder et al. 2015; Sheik-Bahae and Epstein 2007; Stanley et al. 2012).

APPENDIX: THERMODYNAMIC ANALYSIS AND MODELING

Go to:

To provide a framework for interpretation of heat pulse-evoked responses, we analyzed hair cell excitability using a single-compartment model of the form

$$\frac{dQ_m}{dt} + \sum_{j=1}^{J} I_J = I_o, \tag{1}$$

where Q_m is the electrical charge associated with capacitance of the plasma membrane complex, I_j are the ionic currents, and I_o accounts for all other membrane currents, including electrode inputs. Heat pulse-driven electrical excitability arises from temperature-dependent ion channel currents (I_j) and from temperature-dependent membrane capacitance (Q_m), both of which are governed by first principles as described below.

Thermal modulation of membrane capacitance. The capacitive charge Q_m in *Eq. 1* arises from four sources: the lipid bilayer (Fricke 1925; Gorter and Grendel 1925), the ionic double layers present on the two sides of the plasma membrane (Chapman 1913; Gouy 1909; Stern 1924), membrane-bound proteins (Armstrong and Bezanilla 1974; Okunade and Santos-Sacchi 2013; Santos-Sacchi 1991), and other membrane-associated charged macromolecules (Nourse et al. 2014). Time-dependent changes in membrane potential V_m, temperature T, mechanical strain, and/or chemical potentials displace charge within the membrane electric field to generate a displacement current perpendicular to the cell membrane. We consider here only changes in voltage and temperature. The chain rule of calculus provides the capacitive displacement current in the form

$$I_Q = \frac{dQ_m}{dt} = \left(\frac{\partial Q_m}{\partial V_m}\right)\frac{dV_m}{dt} + \left(\frac{\partial Q_m}{\partial T}\right)\frac{dT}{dt}, \tag{2}$$

where V_m is the membrane potential and T is absolute temperature. The coefficient $C_E = \partial Q_m/V_m$ is the well-known electrical capacitance of the cell membrane describing voltage-driven charge displacement, and the coefficient $C_T = \partial Q_m/\partial T$ is the often-neglected thermoelectric capacitance describing temperature-driven charge displacement. Since capacitance scales with membrane surface area, it is useful to normalize both coefficients by the whole cell capacitance C_m^0, measured at a reference temperature T^0. For small changes in temperature $\Delta T = T - T^0$, the total capacitive displacement current from *Eq. 2* can be written

$$\frac{dQ_m}{dt} = C_m^0\left[(1 + \gamma_m \Delta T)\frac{dV_m}{dt} + \lambda_m \frac{dT}{dt}\right], \tag{3}$$

where the electrical capacitance is $C_E = C_m^0(1 + \gamma_m \Delta T)$ and the thermoelectric capacitance is $C_T = C_m^0\lambda_m$. Both γ_m and λ_m are voltage dependent and are related to each other through temperature-dependent electrical properties of the plasma membrane complex. In the present work we determined the thermoelectric capacitance C_T by measuring I_Q in response to temperature commands dT/dt while holding the membrane potential constant ($dV_m/dt \approx 0$), and we determined the electrical capacitance C_E by measuring I_Q in response to voltage commands dV_m/dt while holding temperature constant ($dT/dt \approx 0$).

Hodgkin-Huxley AP simulations.

To simulate generation or extinction of APs by thermal stimuli, we followed the Hodgkin-Huxley approach with temperature dependence of rate constants varying with $Q_{10} = 3$ as detailed by Weiss (1996). The HH model was augmented with thermoelectric capacitance by replacing $C_m(dV_m/dt)$ in the classical model with *Eq. 3*, which introduces a temperature-dependent capacitive current $C_m^0\lambda_m(dT/dt)$ that depolarizes the cell during the IR laser pulse. The thermal transient $T(t)$ was described using *Eq. 28*, driving temperature-dependent ion channel kinetics and thermoelectric capacitive current. Direct current was injected into the model cell to depolarize the neuron to a voltage just below the threshold of firing before the IR heat pulse stimulus was applied. Model equations were solved numerically in the time domain (Mathematica; Wolfram Research, Champaign, IL).

Rapid depolarization driven by thermoelectric capacitance and conductance. For an intense optical heat pulse, the initial temperature rise ΔT can be approximated by a Heaviside step function, $\Delta T \cdot H(t)$, and the rate of temperature change by a Dirac delta function, $dT/dt = \Delta T \cdot \delta(t)$. Inserting these into *Eq. 1* and using *Eq. 3* provides

$$[1 + \gamma_m \Delta T \cdot H(t)] \frac{dV_m}{dt} + \frac{1}{C_m^0} \sum_{j=1}^{J} I_j = -\lambda_m \Delta T \cdot \delta(t). \quad (4)$$

For a pulse duration much shorter than the membrane time constant, integrating this equation over the duration of the pulse gives the whole cell depolarization

$$\Delta V_m \approx -\lambda_m \Delta T - \left(\frac{\Delta t}{2C_m^0}\right) \Delta I_m, \quad (5)$$

where we have used $\gamma_m \Delta T << 1$, and introduced the net heat pulse-evoked membrane conduction current as

$$\Delta I_m = \sum_{j=1}^{J} \Delta I_j.$$

In this equation, ΔT is the temperature rise and Δt is the duration of the heat pulse. The thermoelectric capacitance coefficient λ_m is negative at the cell resting potential, so the term $-\lambda_m \Delta T$ is heat pulse-driven capacitive depolarization associated with membrane electrical charge displacement, a fundamental response present in all cells examined to date (Carvalho-de-Souza et al. 2015; Liu et al. 2014; Shapiro et al. 2012). Whether or not the whole cell is excited or inhibited, however, also depends on the conductance term, which can exceed the capacitive term and carry either sign (see RESULTS AND DISCUSSION). Although the thermoelectric current depends on the rate of temperature rise dT/dt (*Eq. 3*), *Eq. 5* shows that the net whole cell depolarization depends only on the temperature increase ΔT, not the rate of rise (Liu et al. 2014). This holds true providing the thermal pulse is much shorter than the membrane time constant.

One important caveat is that *Eqs. 1–5* assume homogeneous voltage and that the heat pulse acts on the entire cell membrane. Applying a heat pulse to a single dendrite or portion of an axon would substantially reduce the depolarization. This is one reason why application of a heat pulse to a neuronal process rather than the whole cell can be ineffective in evoking action potentials. In myelinated axons, application of the heat pulse locally to a node of Ranvier partially overcomes this challenge but still requires approximately fourfold higher power than whole cell stimulation to compensate for current leak down the axon.

Thermodynamic models of hair cell ion channels.

In type II vestibular hair cells the major ionic channels include delayed rectifiers (K_V, I_{DR}), inward rectifiers (K_{IR}, I_{IR}), inactivating K^+ channels (K_A, I_A) voltage-activated Ca^{2+} channels (Ca_V, I_{CaV}), Ca^{2+}-activated K^+ channels (BK, I_{BK} and SK, I_{SK}), and transient receptor potential channels (TRP, I_{TRP}) (Armstrong and Roberts 2001; Geleoc et al. 2004; Kros et al. 1998; Rusch et al. 1998; Rutherford and Roberts 2009). All of these channels are temperature sensitive, at least to some extent. Classical two-state Hodgkin-Huxley (HH) models (Hodgkin and Huxley 1952; Huxley 1959) are implicitly unable to describe both voltage dependence and temperature dependence simultaneously (Forrest 2014), but this limitation can be overcome in a thermodynamically consistent manner by incorporating additional states, at minimum three states (Latorre et al. 2007; Liu et al. 2003; Sigg et al. 1999; Yang and Gruebele 2003). Using the simplest possible three-state model, we describe gating of a generic channel subunit using a quasi-first-order conformational change

$$Closed_1 \underset{k_{21}}{\overset{k_{12}}{\rightleftharpoons}} Active_2 \underset{k_{32}}{\overset{k_{23}}{\rightleftharpoons}} open_3, \tag{6}$$

where the rate constants k_{nm} are functions of voltage and temperature as described below. Voltage- and ligand-gated activation are modeled by $Closed_1 \leftrightarrow Active_2$, and single-channel kinetics by $Active_2 \leftrightarrow Open_3$. Probabilities of each state are approximated using first-order kinetics. Probability of the closed state was modeled using

$$\frac{dP_1}{dt} = k_{21}P_2 - K_{12}P_1, \tag{7}$$

Probability of the activated state was modeled assuming independent activation and inactivation

$$P_2 = P_2^A P_2^I, \tag{8}$$

where activation kinetics followed the three-state model

$$\frac{dP_2^A}{dt} = k_{12}P_1 - k_{21}P_2 + k_{32}P_3 - k_{23}P_2, \tag{9}$$

and independent slow inactivation followed

$$\frac{dP_2^I}{dt} + \frac{P_2^I + P_2^A - 1}{\tau_I} = 0, \tag{10}$$

where τ_I is the inactivation time constant and $P_2^I = 1$ if inactivation is neglected. Probability of the open state from the three-state model followed

$$\frac{dP_3}{dt} = k_{23}P_2 - k_{32}P_3. \tag{11}$$

Probability P_3 defines the fraction of time the channel is in the open state. Since single -channel kinetics is extremely fast relative to voltage-dependent activation and inactivation, we assumed quasi-

equilibrium of the active and open states, $P_3 \approx (k_{23}/k_{32})P_2 = K_O P_2$. Also, the probabilities of the three states must sum to 1, requiring $P_1 + (1 + K_O)P_2 = 1$. Assuming inactivation is slow, Eq. 9 can be approximated by

$$\frac{dP_2}{dt} + \frac{P_2}{\tau} = \frac{P_2^\infty}{\tau}, \tag{12}$$

revealing the activation time constant as

$$\tau \approx \left(K_O + 1/P_2^I\right) / \left[k_{12}\left(1 + K_O\right) + k_{21}\right], \tag{13}$$

and the steady-state probability that the subunit is in the activated state as

$$P_2^\infty = K_A / \left[1 + K_A(1 + K_O)\right]. \tag{14}$$

Based on thermodynamic considerations described below, the activation equilibrium constant, $K_A = k_{12}/k_{21}$, is temperature, voltage, and ligand sensitive, whereas the single-channel equilibrium constant, $K_O = k_{23}/k_{32}$, is treated as only temperature sensitive. Equations were integrated numerically in the time domain to find P_2, requiring $P_3 = K_O P_2$, $0 \le P_n \le 1$, and $P_1 = 1 - P_2 - P_3$ at each numerical time step, with voltage, ligand, and temperature gating entered through the rate constants as described below.

Assuming n independent subunits must change conformation for channel opening, the open probability is

$$P_{Open} = (K_O P_2)^n, \tag{15}$$

and the channel current is

$$I_j = \overline{G}_j P_{Open}\left(V_m - E_j\right). \tag{16}$$

The form of this model is very similar to the original HH model but differs due to appearance of the single-channel equilibrium constant K_O, gating kinetics, and the thermodynamic form of the rate constants described below.

Thermodynamics of electrical, chemical, and thermal gating. Thermodynamics constrains the relationship between the rate constants and physical stimuli including temperature, mechanical strain, ligand chemical potential, and transmembrane voltage. In the present work we apply first-order transition state theory (Eyring 1935) and write each rate constant in the form

$$k_{nm} = \eta_{nm} e^{-\Delta G_{nm}/RT}, \tag{17}$$

where R is the ideal gas constant, T is absolute temperature, η_{nm} is the base rate, and ΔG_{nm} is the Gibbs free energy change associated with the conformational change $n \rightarrow m$. The Gibbs free energy can be written

$$\Delta G_{nm} = \Delta H_{nm} - T\Delta S_{nm} - z_{nm} F V, \tag{18}$$

where ΔH_{nm} is the change in enthalpy, ΔS_{nm} is the change in entropy, V is the electrical potential difference through which the gating charge moves, z_{nm} is the number of effective gating charges

moving in the electric field per subunit, and F is Faraday's constant. For simplicity, we interpret V as the membrane potential and adjust z_{nm} to account for partial movements and shielded charge.

For voltage-sensitive channels, it is useful to define the activation potential Φ_{nm} as the voltage that balances the change in enthalpy and entropy with the change in voltage rendering $\Delta G_{nm} = 0$:

$$\Phi_{nm} = (\Delta H_{nm} - T\Delta S_{nm})/z_{nm}F. \tag{19}$$

In general, Φ_{nm} can be voltage-dependent, with the first term in a Taylor series expansion defining the standard linear thermodynamic model (Destexhe and Huguenard 2000). The change in entropy can be measured using the half activation voltage at two different temperatures (Correa et al. 1992). In terms of Φ_{nm}, the Gibb's free energy associated with each voltage-sensitive rate constant k_{nm} is

$$\Delta G_{mn} = (\Phi_{nm} - V)z_{nm}F. \tag{20}$$

Combining Eq. 15 with Eq. 12, the forward voltage sensitive rate constant is

$$k_{12} = \eta_{12}e^{-(\Phi_{12}-V)z_{12}F/RT}, \tag{21}$$

and the reverse voltage-sensitive rate constant is

$$k_{21} = \eta_{21}e^{+(\Phi_{21}-V)z_{21}F/RT}, \tag{22}$$

where the sign of the exponent is reversed relative to the forward rate constant due to the opposite direction of charge movement in the electric field. The activation equilibrium constant is the ratio of the two

$$K_A = \frac{k_{12}}{k_{21}} = e^{-(\Phi_A - V)z_A F/RT}, \tag{23}$$

where the half-activation voltage of the channel, $\Phi_A = (\Phi_{12}z_{12} + \Phi_{21}z_{21})/(z_{12} + z_{21})$, is a weighted average of the forward and reverse activation potentials, and the effective gating charge, $z_A = z_{12} + z_{21}$, is the sum of the gating charges in the two directions.

The fast transition from the active state to the open state follows single-channel opening kinetics and is modeled as voltage insensitive ($z_{23} \approx z_{32} \approx 0$). Hence, the opening equilibrium constant can be written

$$K_O = \frac{k_{23}}{k_{32}} = e^{-(\Delta H_O/RT - \Delta S_O/R)}. \tag{24}$$

Notice that changes in temperature alter the equilibrium constant K_O through the difference in enthalpy ΔH_O between the active and open conformations.

For voltage-gated channels, temperature sensitivity also appears in the half-activation voltage Φ_{nm} (Eq. 19) and in the RT denominator of the Gibbs free energy. In our simple three-state model, these two factors enter directly into the voltage-sensitive rate constants and the equilibrium constants K_A and K_O. For ligand-gated channels, assuming quasi-first-order kinetics, ligand concentration enters into the change in the Gibbs free energy through the chemical potential and resulting change in enthalpy. In the case of voltage-sensitive Ca^{2+}-activated channels, Ca^{2+} alters the half-activation voltage and the gating charge displacement rendering the Φ_{nm} and z_{nm} functions of Ca^{2+} concentration: $\Phi_{nm} = \Phi_{nm}(\ln [Ca^{2+}])$ and znm = $z_{nm}(\ln [Ca^{2+}])$. Specific parameters used for simulations of I_{DR} in Fig. 6 were $F = 96{,}485$ C/mol, $R = 8.3145$ J·K^{-1}·mol^{-1}, and $T_0 = 293$°K. For the delayed rectifier, parameters were estimated from experimental data as $z_{12} = z_{21} = 0.6$ (gating charge), $\Phi_{12} = \Phi_{21} = -0.029$ (half-activation

potential), $\eta_{12} = \eta_{21} = 25\ s^{-1}$ (voltage activation time constants), $\Delta H_{12} = \Delta H_{21} = -106$ kJ/mol, $\Delta S_{12} = \Delta S_{21} = -0.356\ kJ \cdot mol^{-1} \cdot °K^{-1}$ (slope and temperature sensitivity of voltage activation), $n = 4$ (independent subunits and decay rate of thermal activation), $E_K = -0.070$ V (K^+ reversal potential), $\Delta H_O = 99$ kJ/mol, $\Delta S_O = -0.343\ kJ \cdot mol^{-1} \cdot °K^{-1}$ (single-channel temperature sensitivity), and $\tau_1 = 3$ s (inactivation time constant). Rates $\eta_{23} = \eta_{32}$ associated with single-channel opening are $>10^4\ s^{-1}$ (Yang and Gruebele 2003) and were treated as instantaneous in the present simulations.

Curve-fitting methods. We quantified the thermoelectric capacitance λ_m by measuring the heat pulse-evoked current in whole cell voltage clamp at fixed membrane potentials. During the fixed-power laser pulse, $dT/dt = r$ is a constant and the temperature rises linearly in time (Liu et al. 2014; Norton and Bowler 2013). Since single-channel gating is very fast, the equilibrium constant K_O can respond almost instantaneously to changes in temperature. As a result, under voltage-clamp conditions when $dV_m/dt = 0$, the whole cell current while the laser pulse is on has a capacitive component proportional to dT/dt and a conductive component proportional to T. For a heat pulse starting at time $t = 0$ with duration t_0, this can be written

$$I(t) = \begin{cases} I = G_m^0 (V_m - E), & t < 0 \\ \lambda_m C_m^0 \frac{dT}{dt} + G_m^0 \left(1 + \frac{t}{\Delta t} \Delta G_m\right)(V_m - E), & 0 < t \le t_0, \\ \left(G_m^0 + \Delta G_m\right)(V_m - E), & t > t_0 \end{cases} \tag{25}$$

where G_m^0 is the whole cell conductance just before the IR heat pulse and E is the whole cell reversal potential. Thermal shifting of the activation potential of each ion channel is limited by voltage-gated opening kinetics (e.g., *Eqs. 12–18*), and therefore rapid changes in conductance arise strictly from ΔG_m associated with rapid changes conductance during the heat pulse. We fit *Eq. 25* to the experimental data at each voltage to extract voltage dependence of the thermoelectric capacitance λ_m and heat pulse-evoked change in conductance ΔG_m.

After major ion channels were blocked, the thermoelectric capacitance was linear with voltage (Fig. 4), consistent with previous reports for lipid bilayers and cell membranes (Carvalho-de-Souza et al. 2015; Shapiro et al. 2012). When ion channels were not blocked, the thermoelectric capacitance reversed sign and increased in slope with cell depolarization. To describe this nonlinearity, we used the heuristic function

$$\lambda_m = \frac{1}{C_m^0} \frac{\partial Q_m}{\partial T} \approx \alpha \left[\frac{1 + (V_m - \psi)/\beta}{\exp\{-(V_m - \psi)/\beta\}} - 1 \right], \tag{26}$$

where α (V/°K) is the gain, β (V) is the voltage sensitivity, and Ψ (V) is the capacitive reversal potential [present α differs from the original report by the whole cell capacitance scaling C_m^0 (Liu et al. 2014)]. Temperature dependence in *Eq. 4* is relatively weak and appears only in the parameter β, which is proportional to absolute temperature; $\beta = \beta^0$, where T is temperature (°K) and β^0 is the voltage sensitivity measured at reference temperature T^0. If $(V_m - \psi)/\beta << 1$, *Eq. 4* reduces to the linear curve sufficient to model membranes and cell lines (Shapiro et al. 2012) but insufficient to capture nonlinearity at depolarized voltages in the present data.

The electrical capacitance is also a function of temperature and membrane potential. Assuming the electrical capacitance arises from membrane-associated mobile charges in series with the lipid, membrane capacitance provides the temperature coefficient as

$$\gamma_m \approx \frac{\alpha}{\beta} \left[\frac{\delta}{2} + \frac{V_m - \psi}{\beta} \mathrm{Sech}\left(\frac{V_m - \psi}{\beta}\right) \mathrm{Tanh}\left(\frac{V_m - \psi}{\beta}\right) \right], \tag{27}$$

where parameters are the same as in *Eq. 4*. The additional nondimensional parameter $\delta \approx 0.1$ is the ratio of the Stern layer thickness to the Debye length. If $(V_m - \psi)/\beta << 1$, *Eq. 27* reduces to a quadratic model, $\gamma_m \approx (\alpha/\beta)[\delta/2 + (V_m - \psi^*)^2/\beta^2]$. The mathematical forms of *Eqs. 26* and *27* are based on Gouy-Chapman-Stern (GCS) theory (Gouy 1909; Chapman 1913; Stern 1924) describing the plasma membrane double layer but have been generalized here by lumping all ions and membrane-bound charged proteins together and expanding for small changes in temperature. This approach renders α, β, and ψ empirically measured parameters dependent on the specific cell, expression levels, and ionic milieu.

Temperature pulse kinetics. A single IR laser pulse (Capella; Lockheed Martin) delivered via a 400-μm-diameter optical fiber (Ocean Optics) increased temperature directly in front of the probe at a rate of 100–652°C/s depending on the laser diode current. Upon cessation of the IR radiation at time $t = t_0$, temperature dissipated and relaxed to media baseline. Temperature relaxation was approximated by a double exponential curve (for more accurate analysis using first principles, see Norton and Bowler 2013; Thompson et al. 2013). Combining heating and relaxation, the temperature transient generated by an IR pulse starting at $t = 0$ and ending at $t = t_0$ was approximated as

$$\Delta T(t) = \begin{cases} 0 & ; \quad t < 0 \\ T_0 \cdot (t/t_0) & ; \quad 0 \le t \le t_0 \\ T_0 \left(\varphi e^{-(t-t_0)/\tau_1} + (1-\varphi) e^{-(t-t_0)/\tau_2} \right) & ; \quad t_0 < t \end{cases}, \tag{28}$$

where $T_0 = t_0(dT/dt)$ is the peak temperature rise at the end of the IR laser pulse, τ_1 and τ_2 are thermal relaxation time constants, and $0 \le \varphi \le 1$ is the relative weighting. Temperature was measured using the change in resistance of a calibrated patch pipette placed in the bath adjacent to the cell (Yao et al. 2009).

The positive rate of temperature change dT/dt during IR heating was more than two orders of magnitude larger than the negative rate during thermal relaxation. Hence, the thermoelectric capacitance C_T was most easily measured during the laser pulse under voltage-clamp conditions when dT/dt was large and $dV/dt = 0$. The electrical capacitance was measured when dT/dt was nearly 0 by commanding dV/dt using a three-sine waveform and recording $I(t)$ as described above.

In a subset of experiments, a sequence of IR pulses were delivered at times $t \in (t_1, t_2, t_3, \ldots, t_N)$. For low pulse rates, we used linear superposition to estimate temperature transients

$$\Delta T_T(t) = \sum_{n=1}^{N} \Delta T(t - t_n). \tag{29}$$

This simple approximation assumes low pulse rates where the volume of tissue heated does not grow substantially in time. For low pulse rates, experimental temperature data were fit with *Eq. 29* and subsequently used in *Eqs. 26* and *27* to estimate capacitance coefficients and membrane parameters α, β, and ψ. Pulse trains were summated to generate tonic increases in temperature with the average steady-state accumulated temperature estimated for low pulse rates from the limit of *Eqs. 28* and *29* as $N \to \infty$.

$$T_\Sigma = T_0\{\varphi/(1 - e^{-\Delta t/\tau_1}) + (1-\varphi)/(1 - e^{-\Delta t/\tau_2}) - 1/2\}, \tag{30}$$

where T_0 is the temperature rise per pulse and $1/\Delta t$ is the pulse rate (pps).

Go to:

GRANTS

This work was supported by National Institute on Deafness and Other Communication Disorders (NIDCD) Grants R01DC011481; and R01DC006685 (to R. D. Rabbitt), Medical Research Council of Australia Grant 1048232 (to A. M. Brichta), the University of Newcastle International Visiting Research Fellowship (to R. Lim), Lockheed Martin Aculight and National Institutes of Health (NIH) Grants R01DC009255; and R01DC002390 (to C. C. Della Santina), and NIH Training Grant T32000023 (to P. J. Boutros).

DISCLOSURES

Go to:

No conflicts of interest, financial or otherwise, are declared by the authors.

AUTHOR CONTRIBUTIONS

Go to:

R.D.R., A.M.B., C.C.D.S., and R.L. conception and design of research; R.D.R., A.M.B., H.T., P.J.B., J.H.A., C.C.D.S., L.P., and R.L. performed experiments; R.D.R., A.M.B., P.J.B., J.H.A., C.C.D.S., and R.L. analyzed data; R.D.R., A.M.B., C.C.D.S., and R.L. interpreted results of experiments; R.D.R., A.M.B., P.J.B., and J.H.A. prepared figures; R.D.R. and A.M.B. drafted manuscript; R.D.R., A.M.B., C.C.D.S., and R.L. edited and revised manuscript; R.D.R., A.M.B., H.T., P.J.B., J.H.A., C.C.D.S., L.P., and R.L. approved final version of manuscript.

REFERENCES

Go to:

Albert ES, Bec JM, Desmadryl G, Chekroud K, Travo C, Gaboyard S, Bardin F, Marc I, Dumas M, Lenaers G, Hamel C, Muller A, Chabbert C. TRPV4 channels mediate the infrared laser-evoked response in sensory neurons. J Neurophysiol 107: 3227–3234, 2012. [PubMed]

Armstrong CE, Roberts WM. Rapidly inactivating and non-inactivating calcium-activated potassium currents in frog saccular hair cells. J Physiol 536: 49–65, 2001. [PMC free article] [PubMed]

Armstrong CM, Bezanilla F. Charge movement associated with the opening and closing of the activation gates of the Na channels. J Gen Physiol 63: 533–552, 1974. [PMC free article] [PubMed]

Arrhenius SA. Über die Dissociationswärme und den Einfluss der Temperatur auf den Dissociationsgrad der Elektrolyte. Z Physik Chem 4: 96–116, 1889.

Baird RA, Desmadryl G, Fernandez C, Goldberg JM. The vestibular nerve of the chinchilla. II. Relation between afferent response properties and peripheral innervation patterns in the semicircular canals. J Neurophysiol 60: 182–203, 1988. [PubMed]

Boyle R, Highstein SM. Resting discharge and response dynamics of horizontal semicircular canal afferents of the toadfish, *Opsanus tau*. J Neurosci 10: 1557–1569, 1990. [PubMed]

Carvalho-de-Souza JL, Treger JS, Dang B, Kent SB, Pepperberg DR, Bezanilla F. Photosensitivity of neurons enabled by cell-targeted gold nanoparticles. Neuron 86: 207–217, 2015. [PMC free article] [PubMed]

Chapman D. A contribution to the theory of electrocapillarity. Philos Mag 25: 475–481, 1913.

Correa AM, Bezanilla F, Latorre R. Gating kinetics of batrachotoxin-modified Na^+ channels in the squid giant axon. Voltage and temperature effects. Biophys J 61: 1332–1352, 1913. [PMC free article] [PubMed]

Curcio J, Petty C. The near infrared absorption spectrum of liquid water. J Opt Soc Am 41: 302–304, 1951.

Destexhe A, Huguenard J. Nonlinear thermodynamic models of voltage-dependent currents. J Comput Neurosci 9: 259–270, 2000. [PubMed]

Dittami GM, Rajguru SM, Lasher RA, Hitchcock RW, Rabbitt RD. Intracellular calcium transients evoked by pulsed infrared radiation in neonatal cardiomyocytes. J Physiol 589: 1295–1306, 2011. [PMC free article] [PubMed]

Duke AR, Jenkins MW, Lu H, McManus JM, Chiel HJ, Jansen ED. Transient and selective suppression of neural activity with infrared light. Sci Rep 3: 2600, 2013. [PMC free article] [PubMed]

Eyring H. The activated complex in chemical reactions. J Chem Phys 3: 107–115, 1935.

Forrest M. Can the thermodynamic Hodgkin-Huxley model of voltage-dependent conductance extrapolate for temperature. Computation 2: 47–60, 2014.

Fricke H. The electric capacity of suspensions with special reference to blood. J Gen Physiol 9: 137–152, 1925. [PMC free article] [PubMed]
Fridberger A, Ren T. Local mechanical stimulation of the hearing organ by laser irradiation. Neuroreport 17: 33–37, 2006. [PubMed]
Galvez A, Gimenez-Gallego G, Reuben JP, Roy-Contancin L, Feigenbaum P, Kaczorowski GJ, Garcia ML. Purification and characterization of a unique, potent, peptidyl probe for the high conductance calcium-activated potassium channel from venom of the scorpion *Buthus tamulus*. J Biol Chem 265: 11083–11090, 1990. [PubMed]
Geleoc GS, Risner JR, Holt JR. Developmental acquisition of voltage-dependent conductances and sensory signaling in hair cells of the embryonic mouse inner ear. J Neurosci 24: 11148–11159, 2004. [PMC free article] [PubMed]
Gorter E, Grendel F. On bimolecular layers of lipoids on the chromocytes of the blood. J Exp Med 41: 439–443, 1925. [PMC free article] [PubMed]
Gouy G. Sur la constitution de la charge électrique à la surface d'un électrolyte. Comput Rend 149, 654–657, 1909.
Hille B. Ionic Channels of Excitable Membranes. Sunderland, MA: Sinauer, 1984.
Hodgkin AL, Huxley AF. A quantitative description of membrane current and its application to conduction and excitation in nerve. J Physiol 117: 500–544, 1952. [PMC free article] [PubMed]
Hodgkin AL, Katz B. The effect of temperature on the electrical activity of the giant axon of the squid. J Physiol 109, 240–249, 1949. [PMC free article] [PubMed]
Hullar TE, Della Santina CC, Hirvonen T, Lasker DM, Carey JP, Minor LB. Responses of irregularly discharging chinchilla semicircular canal vestibular-nerve afferents during high-frequency head rotations. J Neurophysiol 93: 2777–2786, 2005. [PubMed]
Huxley AF. Ion movements during nerve activity. Ann NY Acad Sci 81: 221–246, 1959. [PubMed]
Izzo AD, Richter CP, Jansen ED, Walsh JT Jr. Laser stimulation of the auditory nerve. Lasers Surg Med 38: 745–753, 2006. [PubMed]
Jahn R, Fasshauer D. Molecular machines governing exocytosis of synaptic vesicles. Nature 490: 201–207, 2012. [PMC free article] [PubMed]
Kong WJ, Guo CK, Zhang S, Hao J, Wang YJ, Li ZW. The properties of ACh-induced BK currents in guinea pig type II vestibular hair cells. Hear Res 209: 1–9, 2005. [PubMed]
Kong WJ, Guo CK, Zhang XW, Chen X, Zhang S, Li GQ, Li ZW, Van Cauwenberge P. The coupling of acetylcholine-induced BK channel and calcium channel in guinea pig saccular type II vestibular hair cells. Brain Res 1129: 110–115, 2007. [PubMed]
Kros CJ, Ruppersberg JP, Rusch A. Expression of a potassium current in inner hair cells during development of hearing in mice. Nature 394: 281–284, 1998. [PubMed]
Latorre R, Vargas G, Orta G, Brauchi S. Voltage and temperature gating of thermoTRP channels. In: TRP Ion Channel Function in Sensory Transduction and Cellular Signaling Cascades, edited by Liedtke W, Heller S. Boca Raton, FL: CRC/Taylor and Francis, 2007. [PubMed]
Lee HY, Camp AJ, Callister RJ, Brichta AM. Vestibular primary afferent activity in an in vitro preparation of the mouse inner ear. J Neurosci Methods 145: 73–87, 2005. [PubMed]
Lim R, Kindig AE, Donne SW, Callister RJ, Brichta AM. Potassium accumulation between type I hair cells and calyx terminals in mouse crista. Exp Brain Res 210: 607–621, 2011. [PubMed]
Liu B, Hui K, Qin F. Thermodynamics of heat activation of single capsaicin ion channels VR1. Biophys J 85: 2988–3006, 2003. [PMC free article] [PubMed]
Liu Q, Frerck MJ, Holman HA, Jorgensen EM, Rabbitt RD. Exciting cell membranes with a blistering heat shock. Biophys J 106: 1570–1577, 2014. [PMC free article] [PubMed]
Lumbreras V, Bas E, Gupta C, Rajguru SM. Pulsed infrared radiation excites cultured neonatal spiral and vestibular ganglion neurons by modulating mitochondrial calcium cycling. J Neurophysiol 112: 1246–1255, 2014. [PMC free article] [PubMed]
Lysakowski A, Gaboyard-Niay S, Calin-Jageman I, Chatlani S, Price SD, Eatock RA. Molecular microdomains in a sensory terminal, the vestibular calyx ending. J Neurosci 31: 10101–10114, 2011. [PMC free article] [PubMed]
Lysakowski A, Goldberg JM. A regional ultrastructural analysis of the cellular and synaptic architecture in the chinchilla cristae ampullares. J Comp Neurol 389: 419–443, 1997. [PubMed]

Marlin S, Feldmann D, Nguyen Y, Rouillon I, Loundon N, Jonard L, Bonnet C, Couderc R, Garabedian EN, Petit C, Denoyelle F. Temperature-sensitive auditory neuropathy associated with an otoferlin mutation: deafening fever! Biochem Biophys Res Commun 394: 737–742, 2010. [PubMed]

Minor LB. Gentamicin-induced bilateral vestibular hypofunction. JAMA 279: 541–544, 1998. [PubMed]

Mitsunaga M, Ogawa M, Kosaka N, Rosenblum LT, Choyke PL, Kobayashi H. Cancer cell-selective in vivo near infrared photoimmunotherapy targeting specific membrane molecules. Nat Med 17: 1685–1691, 2011. [PMC free article] [PubMed]

Norton B, Bowler M. Green's function representation of laser induced thermal dynamics and determination of thermal criteria for optically induced neural activation. In: Proc SPIE 8579, Optical Interactions with Tissue and Cells XXIV, 857908, February 15, 2013.

Nourse JL, Prieto JL, Dickson AR, Lu J, Pathak MM, Tombola F, Demetriou M, Lee AP, Flanagan LA. Membrane biophysics define neuron and astrocyte progenitors in the neural lineage. Stem Cells 32: 706–716, 2014. [PMC free article] [PubMed]

Okunade O, Santos-Sacchi J. IR laser-induced perturbations of the voltage-dependent solute carrier protein SLC26a5. Biophys J 105: 1822–1828, 2013. [PMC free article] [PubMed]

Park HJ, Lasker DM, Minor LB. Static and dynamic discharge properties of vestibular-nerve afferents in the mouse are affected by core body temperature. Exp Brain Res 200: 269–275, 2010. [PMC free article] [PubMed]

Paviolo C, Thompson AC, Yong J, Brown WG, Stoddart PR. Nanoparticle-enhanced infrared neural stimulation. J Neural Eng 11: 065002, 2014. [PubMed]

Rajguru SM, Richter CP, Matic AI, Holstein GR, Highstein SM, Dittami GM, Rabbitt RD. Infrared photostimulation of the crista ampullaris. J Physiol 589: 1283–1294, 2011. [PMC free article] [PubMed]

Roder PB, Smith BE, Zhou X, Crane MJ, Pauzauskie PJ. Laser refrigeration of hydrothermal nanocrystals in physiological media. Proc Natl Acad Sci USA 112: 15024–15029, 2015 [PMC free article] [PubMed]

Rodriguez-Ballesteros M, Reynoso R, Olarte M, Villamar M, Morera C, Santarelli R, Arslan E, Meda C, Curet C, Volter C, Sainz-Quevedo M, Castorina P, Ambrosetti U, Berrettini S, Frei K, Tedin S, Smith J, Cruz Tapia M, Cavalle L, Gelvez N, Primignani P, Gomez-Rosas E, Martin M, Moreno-Pelayo MA, Tamayo M, Moreno-Barral J, Moreno F, del Castillo I. A multicenter study on the prevalence and spectrum of mutations in the otoferlin gene (OTOF) in subjects with nonsyndromic hearing impairment and auditory neuropathy. Hum Mutat 29: 823–831, 2008. [PubMed]

Rohmann KN, Wersinger E, Braude JP, Pyott SJ, Fuchs PA. Activation of BK and SK channels by efferent synapses on outer hair cells in high-frequency regions of the rodent cochlea. J Neurosci 35: 1821–1830, 2015. [PMC free article] [PubMed]

Rosenmund C, Stevens CF. Definition of the readily releasable pool of vesicles at hippocampal synapses. Neuron 16: 1197–1207, 1996. [PubMed]

Rusch A, Lysakowski A, Eatock RA. Postnatal development of type I and type II hair cells in the mouse utricle: acquisition of voltage-gated conductances and differentiated morphology. J Neurosci 18: 7487–7501, 1998. [PubMed]

Rutherford MA, Roberts WM. Spikes and membrane potential oscillations in hair cells generate periodic afferent activity in the frog sacculus. J Neurosci 29: 10025–10037, 2009. [PMC free article] [PubMed]

Saito K. Fine structure of the sensory epithelium of the guinea pig organ of Corti: afferent and efferent synapses of hair cells. J Ultrastruct Res 71: 222–232, 1980. [PubMed]

Sans A, Highstein SM. New ultrastructural features in the vestibular labyrinth of the toadfish, *Opsanus tau*. Brain Res 308: 191–195, 1984. [PubMed]

Santos-Sacchi J. Reversible inhibition of voltage-dependent outer hair cell motility and capacitance. J Neurosci 11: 3096–3110, 1991. [PubMed]

Schultz M, Baumhoff P, Maier H, Teudt IU, Kruger A, Lenarz T, Kral A. Nanosecond laser pulse stimulation of the inner ear-a wavelength study. Biomed Opt Express 3: 3332–3345, 2012. [PMC free article] [PubMed]

Shapiro MG, Homma K, Villarreal S, Richter CP, Bezanilla F. Infrared light excites cells by changing their electrical capacitance. Nat Commun 3: 736, 2012. [PMC free article] [PubMed]
Sheik-Bahae M, Epstein RI. Optical refrigeration. Nat Photon 1: 693–699, 2007.
Sigg D, Qian H, Bezanilla F. Kramers' diffusion theory applied to gating kinetics of voltage-dependent ion channels. Biophys J 76: 782–803, 1999. [PMC free article] [PubMed]
Stanley SA, Gagner JE, Damanpour S, Yoshida M, Dordick JS, Friedman JM. Radio-wave heating of iron oxide nanoparticles can regulate plasma glucose in mice. Science 336: 604–608, 2012. [PMC free article] [PubMed]
Starr A, Sininger Y, Winter M, Derebery MJ, Oba S, Michalewski HJ. Transient deafness due to temperature-sensitive auditory neuropathy. Ear Hear 19: 169–179, 1998. [PubMed]
Stern O. Zur Theorie der Elektrolytischen Doppelschicht. Z Elektrochem 30: 508–516, 1924.
Sun DQ, Lehar M, Dai C, Swarthout L, Lauer AM, Carey JP, Mitchell DE, Cullen KE, Della Santina CC. Histopathologic changes of the inner ear in rhesus monkeys after intratympanic gentamicin injection and vestibular prosthesis electrode array implantation. J Assoc Res Otolaryngol 16: 373–387, 2015. [PMC free article] [PubMed]
Sun DQ, Ward BK, Semenov YR, Carey JP, Della Santina CC. Bilateral vestibular deficiency: quality of life and economic implications. JAMA Otolaryngol Head Neck Surg 140: 527–534, 2014. [PMC free article] [PubMed]
Tamm LK, Tatulian SA. Infrared spectroscopy of proteins and peptides in lipid bilayers. Q Rev Biophys 30: 365–429, 1997. [PubMed]
Tan X, Young H, Matic AI, Zirkle W, Rajguru S, Richter CP. Temporal properties of inferior colliculus neurons to photonic stimulation in the cochlea. Physiol Rep 3: e12491, 2015. [PMC free article] [PubMed]
Thompson AC, Fallon JB, Wise AK, Wade SA, Shepherd RK, Stoddart PR. Infrared neural stimulation fails to evoke neural activity in the deaf guinea pig cochlea. Hear Res 324: 46–53, 2015. [PubMed]
Thompson AC, Wade SA, Cadusch PJ, Brown WG, Stoddart PR. Modeling of the temporal effects of heating during infrared neural stimulation. J Biomed Opt 18: 035004, 2013. [PubMed]
Tseeb V, Suzuki M, Oyama K, Iwai K, Ishiwata S. Highly thermosensitive Ca^{2+} dynamics in HeLa cell through IP3 receptors. HFSP J 3: 117–123, 2009. [PMC free article] [PubMed]
Varga R, Avenarius MR, Kelley PM, Keats BJ, Berlin CI, Hood LJ, Morlet TG, Brashears SM, Starr A, Cohn ES, Smith RJ, Kimberling WJ. OTOF mutations revealed by genetic analysis of hearing loss families including a potential temperature sensitive auditory neuropathy allele. J Med Genet 43: 576–581, 2006. [PMC free article] [PubMed]
Wang DY, Wang YC, Weil D, Zhao YL, Rao SQ, Zong L, Ji YB, Liu Q, Li JQ, Yang HM, Shen Y, Benedict-Alderfer C, Zheng QY, Petit C, Wang QJ. Screening mutations of OTOF gene in Chinese patients with auditory neuropathy, including a familial case of temperature-sensitive auditory neuropathy. BMC Med Genet 11: 79, 2010. [PMC free article] [PubMed]
Weiss TF. Cellular Biophysics. Cambridge, MA: MIT Press, 1996.
Wersinger E, Fuchs PA. Modulation of hair cell efferents. Hear Res 279: 1–12, 2011. [PMC free article] [PubMed]
Wersinger E, McLean WJ, Fuchs PA, Pyott SJ. BK channels mediate cholinergic inhibition of high frequency cochlear hair cells. PLoS One 5: e13836, 2010. [PMC free article] [PubMed]
Xie B, Dai C, Li H. Attenuated infrared neuron stimulation response in cochlea of deaf animals may associate with the degeneration of spiral ganglion neurons. Biomed Opt Express 6: 1990–2005, 2015. [PMC free article] [PubMed]
Yang F, Zheng J. High temperature sensitivity is intrinsic to voltage-gated potassium channels. Elife 3: e03255, 2014. [PMC free article] [PubMed]
Yang WY, Gruebele M. Folding at the speed limit. Nature 423: 193–197, 2003. [PubMed]
Yao J, Liu B, Qin F. Rapid temperature jump by infrared diode laser irradiation for patch-clamp studies. Biophys J 96: 3611–3619, 2009. [PMC free article] [PubMed]
Yasunaga S, Grati M, Cohen-Salmon M, El-Amraoui A, Mustapha M, Salem N, El-Zir E, Loiselet J, Petit C. A mutation in OTOF, encoding otoferlin, a FER-1-like protein, causes DFNB9, a nonsyndromic form of deafness. Nat Genet 21: 363–369, 1999. [PubMed]